Supporting Information

Mechanistic Insights into Radical Formation and Functionalization in Copper/*N*-Fluorobenzenesulfonimide Radical-Relay Reactions

Mukunda Mandal,[1,2†*] Joshua A. Buss,[3,4†] Si-Jie Chen,[3,5] Christopher J. Cramer,[1,6] and Shannon S. Stahl[3*]

[1]Department of Chemistry, Chemical Theory Center, and Supercomputing Institute, University of Minnesota, 207 Pleasant Street SE, Minneapolis, MN 55455, United States
[2]Max Planck Institute for Polymer Research, Ackermannweg 10, 55128 Mainz, Germany
[3]Department of Chemistry, University of Wisconsin-Madison, 1101 University Avenue, Madison, WI 53706, United States
[4]Current address: Department of Chemistry, University of Michigan, Ann Arbor, MI 48109, United States
[5]Current address: Department of Discovery Chemistry, Merck & Co. Inc., South San Francisco, CA 93080, United States
[6]Current address: Underwriters Laboratories Inc., 333 Pfingsten Road, Northbrook, IL 60602, United States

[†]These authors contributed equally to this work.

*Email: mukunda.chem@gmail.com, stahl@chem.wisc.edu

Table of Contents

1. Experimental selectivity studies

The data for the isobutylbenzene and isopentylbenzene test substrates has been published elsewhere in earlier reports of benzylic etherification[1] and chlorination.[2] Representative procedures for 4-ethyltoluene are included here.

Etherification: A 4 mL septa-capped glass vial was charged with CuCl (10 mol %, 0.02 mmol, 2.0 mg), 2, 2'-bisoxazoline (10 mol %, 0.02 mmol, 2.8 mg) and NFSI (2.0 equiv., 0.4 mmol, 126.1 mg) and a stir bar. The vial was sealed and the headspace sparged with dinitrogen for 30 seconds. A stock solution of alkylbenzene (1.0 equiv., 0.2 mmol), MeOH (5.0 equiv., 1.0 mmol, 40.5 μL) and diisopropyl phosphite (0.5 equiv., 0.1 mmol, 16.7 μL) in CH_2Cl_2:HFIP = 4:1 (0.2 M, 1.0 mL) was injected through the septum cap. The reaction mixture was heated at 40 °C and stirred for 16 hours.

At this time, the reaction was filtered through a silica plug (*ca.* 3" in a 9" Pasteur pipette). The vial was rinsed with an additional CH_2Cl_2 (3 mL), which was passed through the plug and mesitylene (28 μL, 0.2 mmol, 1.0 equiv.) was added into the combined filtrates. An aliquot of the filtrates was taken up in $CDCl_3$ (*ca.* 1 mL) and a 400 μL aliquot was transferred to an NMR tube for analysis.

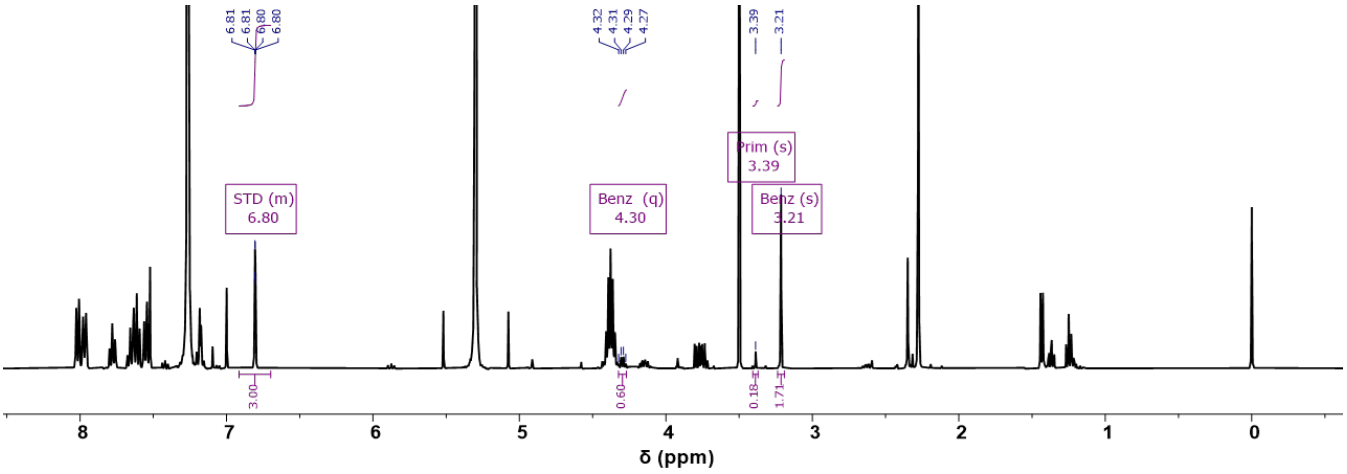

Figure S1. ^{1}H NMR Spectrum (400 MHz, 24 °C, $CDCl_3$) of a representative Cu/NFSI methoxylation of 4-ethyltoluene (crude). The diagnostic peaks for 2° benzylic (Benz–5.07 ppm), 1° benzylic (Prim–2.70 ppm), dichlorination (1°/2° Cl2–5.02 ppm), and unreacted starting material (SM–2.60 ppm) are labeled accordingly.

Ag/^{t}BuOCl: A 4 mL septa-capped scintillation vial was charged with 4-ethyltoluene (145 μL, 1.0 mmol, 1 equiv.) and a stir bar. The vial was sealed and the headspace sparged with dinitrogen for 30 seconds. A stock solution of Ag(phen)OTf in anhydrous MeCN (400 μL, 5.5 mM, 0.002 equiv.) was injected through the septum cap.[3] Neat ^{t}BuOCl (225 μL, 2.0 μmol, 2.0 equiv.) was then injected and the reaction mixture left to stir for 48 hours.

At this time, the reaction was diluted with EtOAc (0.5 mL) and filtered through a silica plug (*ca.* 3" in a 9" Pasteur pipette). The vial was rinsed with an additional portion of EtOAc (0.5 mL) which was likewise passed through the plug. The combined filtrates were dried under reduced pressure and the resulting residue was taken up in $CDCl_3$ (*ca.* 1 mL), mesitylene (30 μL, 0.22 mmol, 0.22 equiv.) was added, and a 400 μL aliquot was transferred to an NMR tube for analysis.

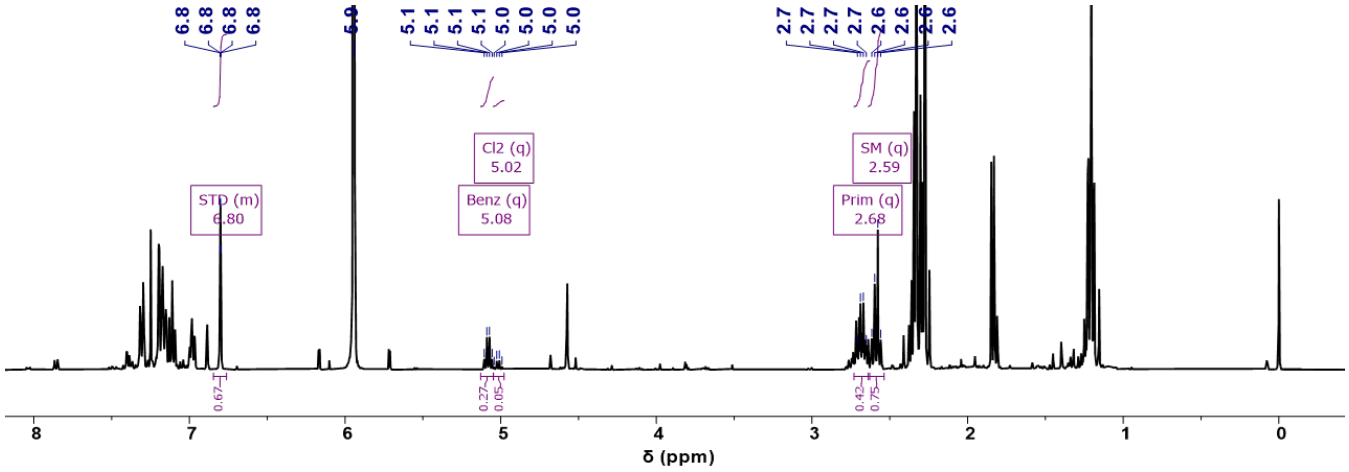

Figure S2. ^{1}H NMR Spectrum (400 MHz, 24 °C, $CDCl_3$) of a representative Ag/^{t}BuOCl chlorination of 4-ethyltoluene (crude). The diagnostic peaks for 2° benzylic (Benz–5.07 ppm), 1° benzylic (Prim–2.70 ppm), dichlorination (1°/2° Cl2–5.02 ppm), and unreacted starting material (SM–2.60 ppm) are labeled accordingly.

SO_2Cl_2: A 4 mL septa-capped scintillation vial was charged with 4-ethyltoluene (145 µL, 1.0 mmol, 1 equiv.), a stock solution of bis(benzoyl)peroxide in chlorobenzene (250 µL, 0.04 M, 0.01 equiv.), and a stir bar. The vial was sealed and the contents sparged with dinitrogen for 30 seconds. SO_2Cl_2 (80 µL, 1.0 mmol, 1 equiv.) was injected through the septum cap and the vial placed in a pre-heated 75 °C aluminum block. Stirring was initiated and the reaction was left for 4 hours.

At this time, the reaction was cooled to room temperature, diluted with chlorobenzene (0.5 mL) and filtered through a silica plug (*ca.* 3" in a 9" Pasteur pipette). The vial was rinsed with additional portions of chlorobenzene (0.5 mL × 2) which was likewise passed through the plug. Mesitylene (30 µL, 0.22 mmol, 0.22 equiv.) was added to the combined filtrates as an internal standard. A 30 µL aliquot was transferred to an NMR tube, diluted with $CDCl_3$ (500 µL), and analyzed by ^{1}H NMR spectroscopy.

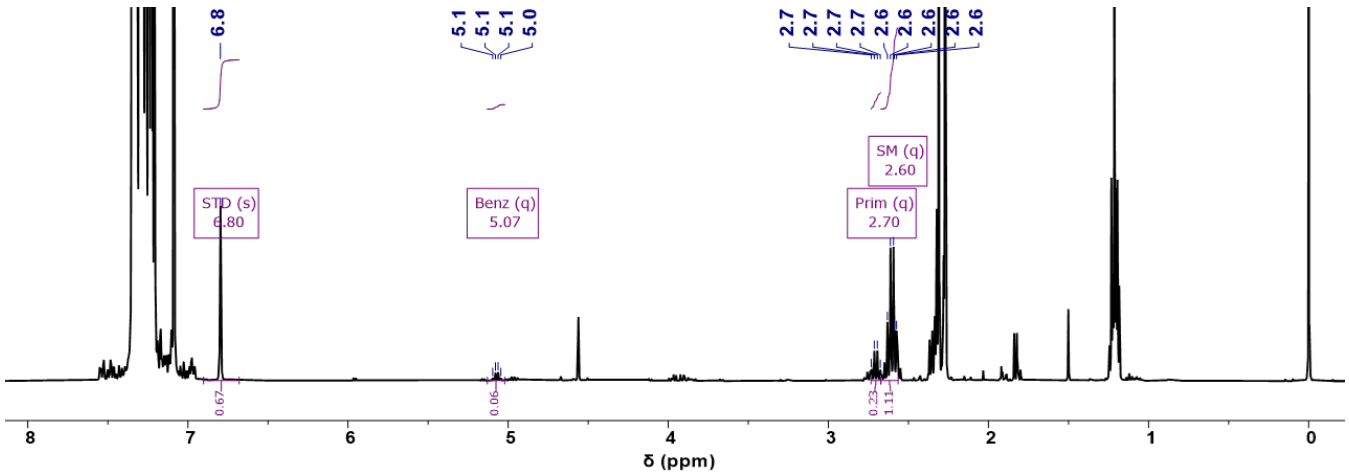

Figure S3. ^{1}H NMR Spectrum (400 MHz, 24 °C, $CDCl_3$) of a representative SO_2Cl_2 chlorination of 4-ethyltoluene (crude). The diagnostic peaks for 2° benzylic (Benz–5.07 ppm), 1° benzylic (Prim–2.70 ppm), and unreacted starting material (SM–2.60 ppm) are labeled accordingly.

Table S1. Summary of chlorination results.

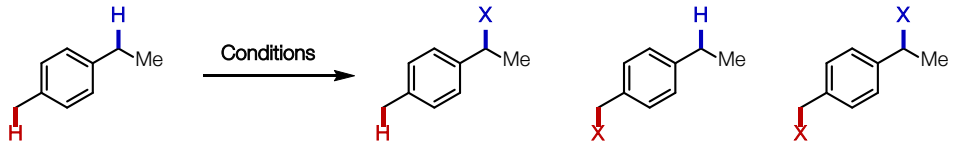

	SM	2° C–H	1° C–H	Difunctionalization	2° Benzylic Selectivity
Cu/NFSI Methoxylation	--	60	6	--	91%
Ag/^{t}BuOCl Chlorination	37	27	21	5	56%
SO_2Cl_2 Chlorination	55	6	12	--	33%

2. Crystallographic data

2.1. Crystal growth

In a dinitrogen glovebox, a 2 mL scintillation vial was charged with bathophenanthroline (33.24 mg, 0.1 mmol, 1 equiv.) [Sigma Aldrich], dibenzenesulfonamide (59.4 mg, 0.2 mmol, 2 equiv.) [TCI], copper(II) fluoride dihydrate (13.8 mg, 0.1 mmol, 1 equiv.) [Sigma Aldrich], and a magnetic stir bar. Chlorobenzene (1 mL) was added, and the vial was sealed with a septum cap. The reaction was removed from the glovebox and stirred at 50 °C for 12 hours. Upon cooling, blue microcrystals were observed to precipitate from a deep green solution.

In a chemical fume hood (without exclusion of moisture or air), the solids were collected via filtration through a glass microfiber and taken up in minimal dichloromethane, giving a green solution. Vapor diffusion of pentane into this concentrated DCM solution afforded single crystals of BphenCu(NSI)(Cl) suitable for X-ray diffraction studies, as described in detail below.

2.2. Data collection

A colorless crystal with approximate dimensions 0.0.9 × 0.06 × 0.03 mm^3 was selected under oil under ambient conditions and attached to the tip of a MiTeGen MicroMount©. The crystal was mounted in a stream of cold nitrogen at 100(1) K and centered in the X-ray beam by using a video camera.

The crystal evaluation and data collection were performed on a Bruker Quazar SMART APEXII diffractometer with Mo K_α (λ = 0.71073 Å) radiation and the diffractometer to crystal distance of 4.96 cm.[4]

The initial cell constants were obtained from three series of ω scans at different starting angles. Each series consisted of 12 frames collected at intervals of 0.5° in a 6° range about ω with the exposure time of 60 seconds per frame. The reflections were successfully indexed by an automated indexing routine built in the APEXII program suite. The final cell constants were calculated from a set of 5769 strong reflections from the actual data collection.

The data were collected by using the full sphere data collection routine to survey the reciprocal space to the extent of a full sphere to a resolution of 0.75 Å. A total of 21819 data were harvested by collecting 4 sets of frames with

0.4° scans in ω and φ with exposure times of 90 sec per frame. These highly redundant datasets were corrected for Lorentz and polarization effects. The absorption correction was based on fitting a function to the empirical transmission surface as sampled by multiple equivalent measurements.[5]

2.3. Structure solution and refinement

The diffraction data were consistent for the space groups $P\bar{1}$ and $P1$. The *E*-statistics strongly suggested the centrosymmetric space group $P\bar{1}$ that yielded chemically reasonable and computationally stable results of refinement.[6–9]

A successful solution by the direct methods provided most non-hydrogen atoms from the *E*-map. The remaining non-hydrogen atoms were located in an alternating series of least-squares cycles and difference Fourier maps. All non-hydrogen atoms were refined with anisotropic displacement coefficients. All hydrogen atoms were included in the structure factor calculation at idealized positions and were allowed to ride on the neighboring atoms with relative isotropic displacement coefficients.

There were several peaks of electron density in the structure that corresponded to solvent molecules of dichloromethane and pentane. It is likely that these solvent molecules are disordered over several positions and therefore have electron density that is diffuse. A significant amount of time was invested in identifying and refining the disordered molecules. Bond length constraints were applied to model the molecules, but the resulting isotropic displacement coefficients suggested the molecules were mobile. In addition, the refinement was computationally unstable. Option SQUEEZE of program PLATON was used to correct the diffraction data for diffuse scattering effects and to identify the solvate molecule.[10] PLATON calculated the upper limit of volume that can be occupied by the solvent to be 153 $Å^3$, or 9.1% of the unit cell volume. The program calculated 53 electrons in the unit cell for the diffuse species. This approximately corresponds to 1.25 molecules of solvent, where this solvent may be DCM, pentane, or a combination of the two, in the unit cell (52.5 electrons). Please note that all derived results in the following tables are based on the known contents. No data are given for the diffusely scattering species.

The final least-squares refinement of 424 parameters against 8335 data resulted in residuals *R* (based on F^2 for $I \geq 2\sigma$) and *wR* (based on F^2 for all data) of 0.0397 and 0.1002, respectively. The final difference Fourier map was featureless.

2.4. Summary

Crystal Data for $C_{36}H_{26}ClCuN_3O_4S_2$ (M =727.71 g/mol): triclinic, space group $P\bar{1}$ (no. 2), a = 10.232(3) Å, b = 10.735(4) Å, c = 16.557(8) Å, α = 85.248(14)°, β = 72.999(17)°, γ = 74.424(14)°, V = 1675.3(11) Å^3, Z = 2, T = 99.99 K, μ(Mo K$_\alpha$) = 0.900 mm^{-1}, *Dcalc* = 1.443 g/cm^3, 21819 reflections measured (2.572° ≤ 2Θ ≤ 56.714°), 8335 unique (R_{int} = 0.0381, R_{sigma} = 0.0523) which were used in all calculations. The final R_1 was 0.0397 (I > 2σ(I)) and wR_2 was 0.1002 (all data).

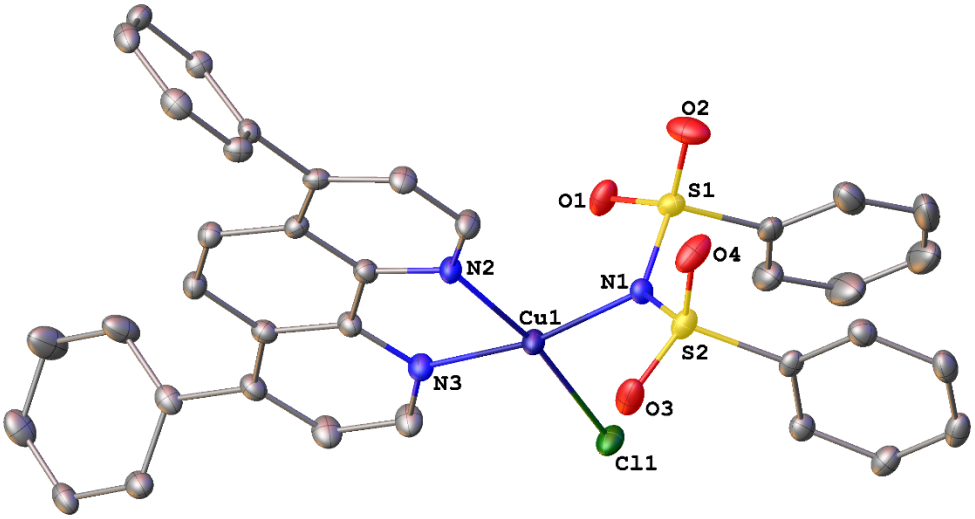

Figure S4. A molecular drawing of [(BPhen)Cu^{II}(Cl)(NSI)] (BPhen = Bathophenanthroline; NSI = *N*-sulfonimidyl) shown with 50% probability ellipsoids. All H atoms are omitted.

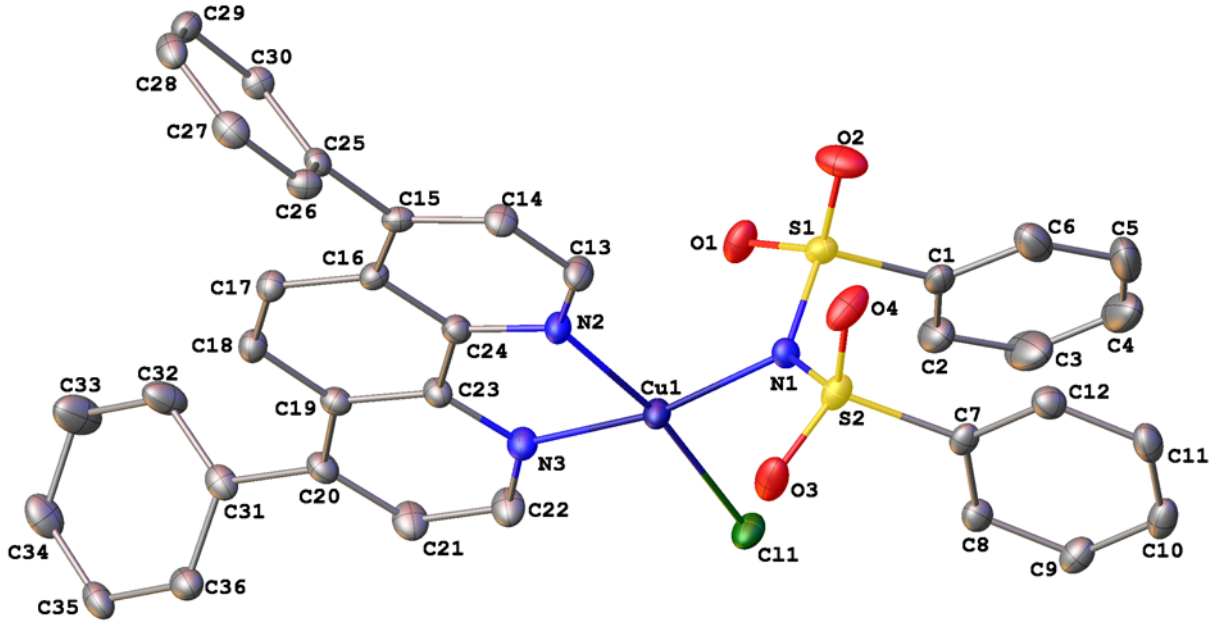

Figure S5. A molecular drawing of [(BPhen)Cu^{II}(Cl)(NSI)] shown with 50% probability ellipsoids and all non–H atoms labeled. All H atoms are omitted.

Table S2. Crystal data and structure refinement for [(BPhen)Cu^{II}(Cl)(NSI)].

Empirical formula	$C_{36}H_{26}ClCuN_3O_4S_2$
Formula weight	727.71
Temperature/K	99.99
Crystal system	triclinic
Space group	$P\bar{1}$
a/Å	10.232(3)
b/Å	10.735(4)
c/Å	16.557(8)
α/°	85.248(14)
β/°	72.999(17)
γ/°	74.424(14)
Volume/Å^3	1675.3(11)
Z	2
ρ_{calc}/g cm^{-3}	1.443
μ/mm^{-1}	0.900
F(000)	746.0
Crystal size/mm^3	0.09 × 0.06 × 0.03
Radiation	Mo K_α (λ = 0.71073)
2Θ range for data collection/°	2.572 to 56.714
Index ranges	−13 ≤ h ≤ 13, −13 ≤ k ≤ 14, −22 ≤ l ≤ 22
Reflections collected	21819
Independent reflections	8335 [R_{int} = 0.0381, R_{sigma} = 0.0523]
Data/restraints/parameters	8335/0/424
Goodness-of-fit on F^2	1.032
Final R indexes [I>=2σ (I)]	R_1 = 0.0397, wR_2 = 0.0934
Final R indexes [all data]	R_1 = 0.0599, wR_2 = 0.1002
Largest diff. peak/hole / e Å^{-3}	0.62/−0.61

3. "Correction" to calculated Gibbs free energy due to standard-state concentration changes

We note that the thermal contributions to Gibbs free energies were calculated in the gas phase, where the standard state is 1 atm pressure. Using the ideal gas law (PV = nRT), we can determine the concentration (c) in the gas phase: c = n/V = P/RT. Therefore, at 298 K, the concentration in the gas phase is approximately 1 mole per 24.46 L, which is significantly more dilute than the standard state concentration in solution, which is 1 mole per 1 L. The loss of translational entropy associated with transferring 1 mole of gas from 24.46 L to 1 L can be calculated as RT*ln(24.46), where T is 298 K. This calculation yields a value of approximately 1.89 kcal/mol. This concentration correction term was added to the absolute free energies of all the computed species.

4. Cartesian coordinates of DFT computed structures

Cartesian coordinates of all DFT-optimized structures can be accessed from the coordinate file (.xyz).

5. Structures of 'small' species involved in the study and their energetics

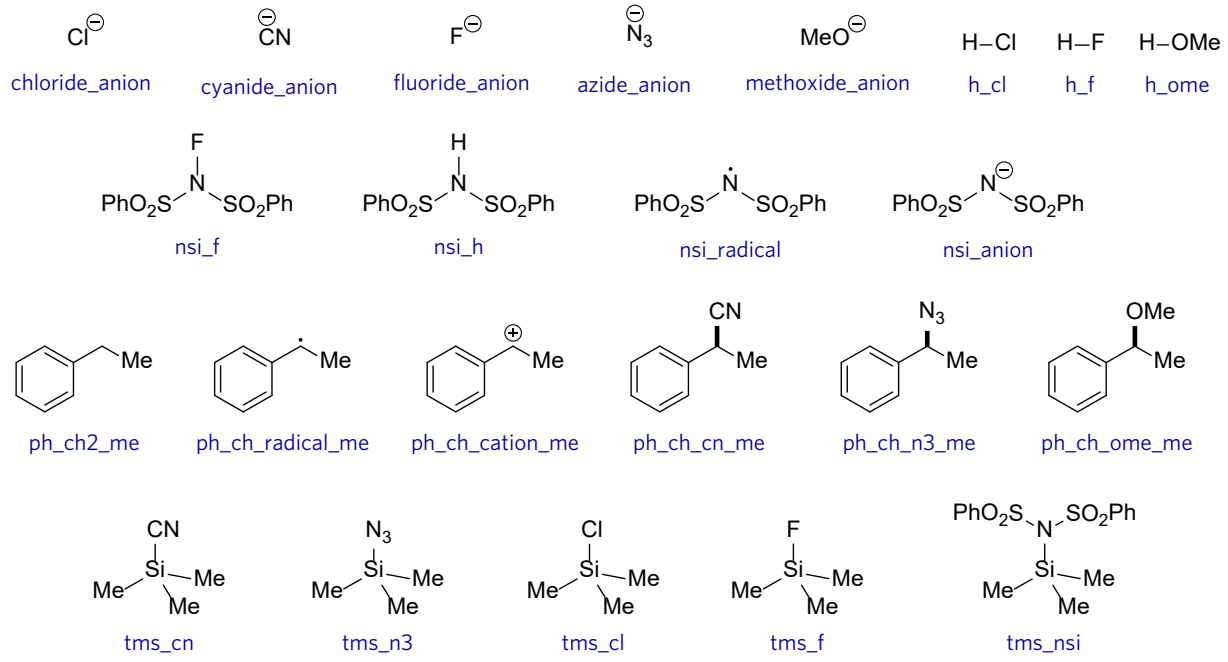

Figure S6. Line drawing of the structures, the energetics of which are shown in **Table S3**.

Table S3. Electronic energies, Gibbs free energies (G) and thermal contribution to G for structures shown in **Figure S6**. Energies are reported in hartree computed at M06-D3(0)/basis-II/SMD(DCM)//M06-D3(0)/basis-I level of theory at 298.15 K.

File/Structure name	Electronic energy (hartree)	Thermal contribution to *G* (hartree)	Gibbs free energy (*G*, hartree)
chloride_anion	-460.3566184	-0.015023	-460.3686214
cyanide_anion	-92.92258794	-0.014065	-92.93363294
fluoride_anion	-99.9827974	-0.014159	-99.9939364
azide_anion	-164.2910419	-0.005229	-164.2932509
methoxide_anion	-115.1754287	0.014324	-115.1580847
h_cl	-460.8009944	-0.011116	-460.8090904
h_f	-100.4647966	-0.006813	-100.4685896
h_ome	-115.7057932	0.028262	-115.6745112
nsi_f	-1714.86359	0.163969	-1714.696601
nsi_h	-1615.703549	0.172178	-1615.528351
nsi_radical	-1615.022297	0.157542	-1614.861735
nsi_anion	-1615.248438	0.161729	-1615.083689
ph_ch2_me	-310.7432788	0.123488	-310.6167708
ph_ch_radical_me	-310.098379	0.108837	-309.986522
ph_ch_cation_me	-309.928012	0.112352	-309.81264
ph_ch_cn_me	-402.9654835	0.120144	-402.8423195
ph_ch_n3_me	-474.30557	0.123343	-474.179207
ph_ch_ome_me	-425.2485005	0.152817	-425.0926635
tms_cn	-502.043427	0.083668	-501.956739
tms_n3	-573.4156522	0.08705	-573.3255822
tms_cl	-869.467307	0.077618	-869.386669
tms_f	-509.1372918	0.079341	-509.0549308
tms_nsi	-2024.354047	0.265367	-2024.08566

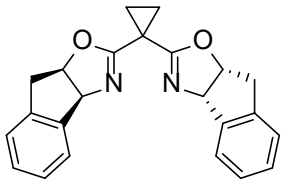

bare_ligand

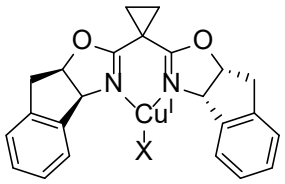

X =

- Cl (cu_i_cl_wLig)
- CN (cu_i_cn_wLig)
- F (cu_i_f_wLig)
- N_3 (cu_i_n3_wLig)
- OMe (cu_i_ome_wLig)
- NSI (cu_i_nsi_wLig)

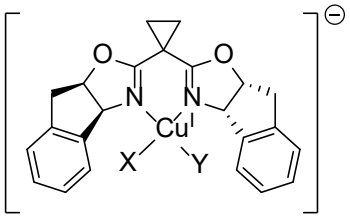

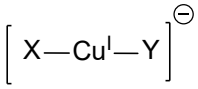

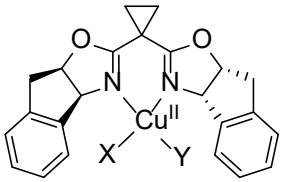

X	Y	file_name	file_name	file_name
Cl	F	cu_i_cl_f_anion_wLig	cu_i_cl_f_anion_noLig	cu_ii_cl_f_wLig
Cl	CN	cu_i_cl_cn_anion_wLig	cu_i_cl_cn_anion_noLig	cu_ii_cl_cn_wLig
Cl	N_3	cu_i_cl_n3_anion_wLig	cu_i_cl_n3_anion_noLig	cu_ii_cl_n3_wLig
Cl	OMe	cu_i_cl_ome_anion_wLig	cu_i_cl_ome_anion_noLig	cu_ii_cl_ome_wLig
CN	CN	cu_i_cn_cn_anion_wLig	cu_i_cn_cn_anion_noLig	cu_ii_cn_cn_wLig
N_3	N_3	cu_i_n3_n3_anion_wLig	cu_i_n3_n3_anion_noLig	cu_ii_n3_n3_wLig
OMe	OMe	cu_i_ome_ome_anion_wLig	cu_i_ome_ome_anion_noLig	cu_ii_ome_ome_wLig
NSI	Cl	cu_i_nsi_cl_anion_wLig	cu_i_nsi_cl_anion_noLig	cu_ii_nsi_cl_wLig
NSI	CN	cu_i_nsi_cn_anion_wLig	cu_i_nsi_cn_anion_noLig	cu_ii_nsi_cn_wLig
NSI	N_3	cu_i_nsi_n3_anion_wLig	cu_i_nsi_n3_anion_noLig	cu_ii_nsi_n3_wLig
NSI	OMe	cu_i_nsi_ome_anion_wLig	cu_i_nsi_ome_anion_noLig	cu_ii_nsi_ome_wLig
F	CN	--	--	cu_ii_f_cn_wLig
F	N_3	--	--	cu_ii_f_n3_wLig
F	OMe	--	--	cu_ii_f_ome_wLig

Figure S7. Line drawing of the structures, the energetics of which are shown in **Table S4**.

Table S4. Electronic energies, Gibbs free energies (G) and thermal contribution to G for structures shown in **Figure S7**. Energies are reported in hartree computed at M06-D3(0)/basis-II/SMD(DCM)//M06-D3(0)/basis-I level of theory at 298.15 K.

File/Structure name	Electronic energy (hartree)	Thermal contribution to *G* (hartree)	Gibbs free energy (*G*, hartree)
bare_ligand	-1148.054231	0.331746	-1147.719465
cu_i_cl_wLig	-3248.867115	0.32971	-3248.534385
cu_i_cn_wLig	-2881.454109	0.335841	-2881.115248
cu_i_f_wLig	-2888.490469	0.331158	-2888.156291
cu_i_n3_wLig	-2952.802895	0.339553	-2952.460322
cu_i_ome_wLig	-2903.708631	0.367198	-2903.338413
cu_i_nsi_wLig	-4403.764756	0.51877	-4403.242966
cu_i_cl_f_anion_wLig	-3348.845709	0.325324	-3348.517365
cu_i_cl_cn_anion_wLig	-3341.810759	0.331034	-3341.476705
cu_i_cl_n3_anion_wLig	-3413.164522	0.334845	-3412.826657
cu_i_cl_ome_anion_wLig	-3364.065486	0.363079	-3363.699387
cu_i_cn_cn_anion_wLig	-2974.395227	0.337769	-2974.054438
cu_i_n3_n3_anion_wLig	-3117.102774	0.345755	-3116.753999
cu_i_ome_ome_anion_wLig	-3018.909199	0.399839	-3018.50634
cu_i_nsi_cl_anion_wLig	-4864.142238	0.518854	-4863.620364
cu_i_nsi_cn_anion_wLig	-4496.730502	0.524223	-4496.203259
cu_i_nsi_n3_anion_wLig	-4568.080933	0.528012	-4567.549901
cu_i_nsi_ome_anion_wLig	-4518.986496	0.557431	-4518.426045
cu_i_cl_f_anion_noLig	-2200.793025	-0.02419	-2200.814195
cu_i_cl_cn_anion_noLig	-2193.751388	-0.018774	-2193.767142
cu_i_cl_n3_anion_noLig	-2265.10091	-0.017388	-2265.115278
cu_i_cl_ome_anion_noLig	-2216.007429	0.009145	-2215.995264
cu_i_cn_cn_anion_noLig	-1826.33348	-0.006901	-1826.337361
cu_i_n3_n3_anion_noLig	-1969.035998	-0.008508	-1969.041486
cu_i_ome_ome_anion_noLig	-1870.849378	0.044464	-1870.801894
cu_i_nsi_cl_anion_noLig	-3716.0521	0.157846	-3715.891234
cu_i_nsi_cn_anion_noLig	-3348.63815	0.163664	-3348.471466
cu_i_nsi_n3_anion_noLig	-3419.987681	0.167222	-3419.817439
cu_i_nsi_ome_anion_noLig	-3370.894047	0.193893	-3370.697134
cu_ii_form_nfsi_TS_brk_symS_cnf1	-4963.7242059	0.5187340	-4963.2024519
cu_ii_form_nfsi_TS_brk_symS_cnf2	-4963.7296482	0.5173140	-4963.2093142
cu_ii_cl_f_wLig	-3348.720527	0.332203	-3348.385304
cu_ii_cl_cn_wLig	-3341.664771	0.335583	-3341.326168
cu_ii_cl_n3_wLig	-3413.027934	0.339519	-3412.685395
cu_ii_cl_ome_wLig	-3363.946076	0.367501	-3363.575555
cu_ii_cn_cn_wLig	-2974.244037	0.341096	-2973.899921
cu_ii_n3_n3_wLig	-3116.970593	0.350062	-3116.617511
cu_ii_ome_ome_wLig	-3018.800645	0.406324	-3018.391301
cu_ii_nsi_cl_wLig	-4863.973235	0.52058	-4863.449635
cu_ii_nsi_cn_wLig	-4496.553776	0.52611	-4496.024646
cu_ii_nsi_n3_wLig	-4567.911648	0.531343	-4567.377285
cu_ii_nsi_ome_wLig	-4518.835813	0.559404	-4518.273389
cu_ii_f_cn_wLig	-2981.300857	0.337911	-2980.959926
cu_ii_f_n3_wLig	-3052.664534	0.342261	-3052.319253
cu_ii_f_ome_wLig	-3003.581434	0.370152	-3003.208262

6. All ligand exchange energetics

Table S5. Ligand exchange energetics starting from two key Cu^{II} resting states: $LCu^{II}(Cl)(F)$ and $LCu^{II}(Cl)(NSI)$. Gibbs free energies (kcal/mol) are computed at M06-D3(0)/basis-II/SMD(DCM)//M06-D3(0)/basis-I level of theory at 298.15 K. Solid lines indicate the energetically favored route (energetics are highlighted in blue), while dashed lines indicate the alternative ligand exchange route.

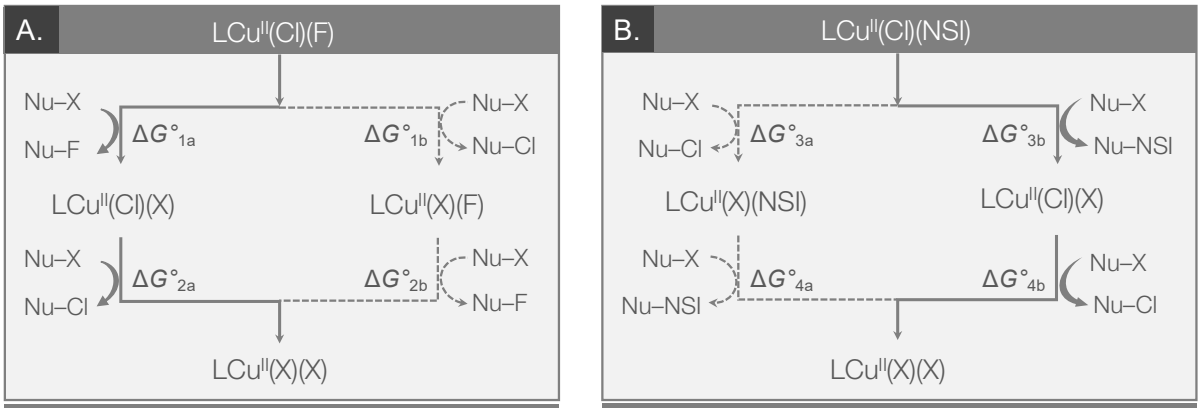

X	$\Delta G°_{1a}$	$\Delta G°_{1b}$	$\Delta G°_{2a}$	$\Delta G°_{2b}$
CN	–24.5	–2.9	–2.3	–24.0
N_3	–18.5	3.1	4.3	–17.3
OMe	9.8	26.6	31.2	14.4

X	$\Delta G°_{3a}$	$\Delta G°_{3b}$	$\Delta G°_{4a}$	$\Delta G°_{4b}$
CN	–3.1	–3.4	–2.6	–2.3
N_3	7.1	2.6	–0.2	4.3
OMe	26.1	12.7	17.7	31.2

7. Favored reduced state of various LCu^{II} species

Table S6. Four possible routes for the oxidation of a benzyl radical into a benzyl cation by an LCu^{II} species. Gibbs free energies (kcal/mol) are computed at M06-D3(0)/basis-II/SMD(DCM)//M06-D3(0)/basis-I level of theory at 298.15 K. In each case, the energetically favored route is highlighted in blue.

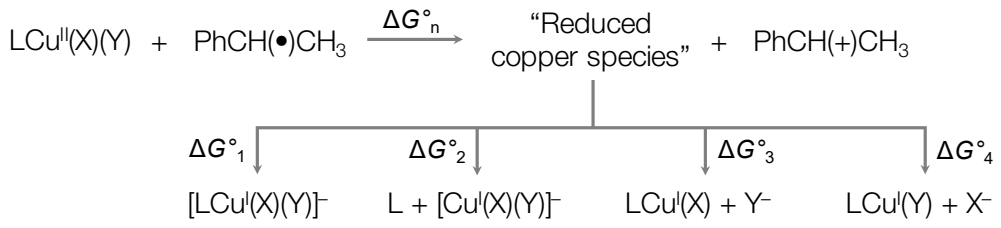

$LCu^{II}(X)(Y)$ Species	$[LCu^{I}(X)(Y)]^-$ $\Delta G_1°$	$L + [Cu^{I}(X)(Y)]^-$ $\Delta G_2°$	$LCu^{I}(X) + Y^-$ $\Delta G_3°$	$LCu^{I}(Y) + X^-$ $\Delta G_4°$
$LCu^{II}(Cl)(F)$	26.2	16.0	19.4	21.5
$LCu^{II}(Cl)(CN)$	14.6	8.4	20.1	10.2
$LCu^{II}(Cl)(N_3)$	20.5	15.4	19.9	19.0
$LCu^{II}(Cl)(OMe)$	31.4	21.8	35.7	26.6
$LCu^{II}(CN)(CN)$	12.2	10.7	15.6	15.6
$LCu^{II}(N_3)(N_3)$	23.5	19.1	23.7	23.7
$LCu^{II}(OMe)(OMe)$	36.9	27.5	43.1	43.1
$LCu^{II}(NSI)(Cl)$	2.0	8.0	7.5	3.4
$LCu^{II}(NSI)(CN)$	–3.0	4.8	13.8	–0.3
$LCu^{II}(NSI)(N_3)$	0.8	9.0	9.4	4.5
$LCu^{II}(NSI)(OMe)$	13.3	19.2	29.0	15.8

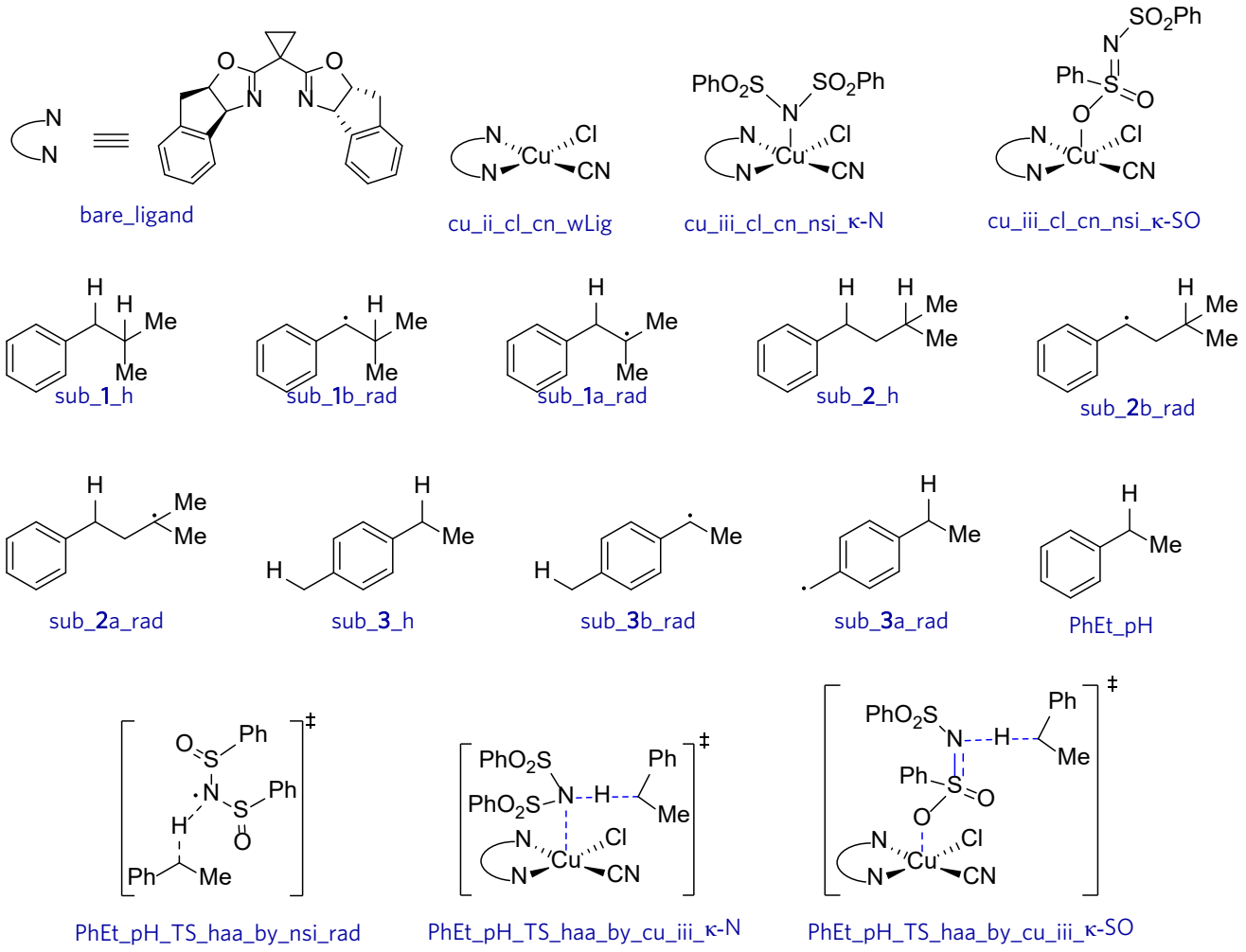

Figure S8. Line drawing of the structures, the energetics of which are shown in **Table S7.**

Table S7. Electronic energies, Gibbs free energies (G) and thermal contribution to G for structures shown in Figure S8. Energies are reported in hartree computed at M06-D3(0)/basis-II/SMD(DCM)//M06-D3(0)/basis-I level of theory at 298.15 K.

File/Structure name	Electronic energy (hartree)	Thermal contribution to *G* (hartree)	Gibbs free energy (*G*, hartree)
nsi_radical	-1615.022297	0.157542	-1614.861735
cu_ii_cl_cn_wLig	-3341.664771	0.335583	-3341.326168
cu_iii_cl_cn_nsi_κ-N_RS	-4956.7273112	0.5287630	-4956.1955282
cu_iii_cl_cn_nsi_κ-N_brk_symS	-4956.704249†	0.5252400	-4956.1759898
cu_iii_cl_cn_nsi_κ-N_T	-4956.7068440	0.5246150	-4956.1792090
cu_iii_cl_cn_nsi_κ-SO_RS	-4956.7337645	0.5286310	-4956.2021135
cu_iii_cl_cn_nsi_κ-SO_brk_symS	-4956.710175†	0.5223460	-4956.1848096
cu_iii_cl_cn_nsi_κ-SO_T	-4956.7104931	0.5224370	-4956.1850361

sub_1_h	-389.3375372	0.176965	-389.1575522
sub_1b_rad	-388.6905559	0.162152	-388.5253839
sub_1a_rad	-388.6799161	0.160834	-388.5160621
sub_2_h	-428.6339164	0.202197	-428.4286994
sub_2b_rad	-427.988414	0.188536	-427.796858
sub_2a_rad	-427.9749652	0.185375	-427.7865702
sub_3_h	-350.0425106	0.147562	-349.8919286
sub_3b_rad	-349.398152	0.132826	-349.262306
sub_3a_rad	-349.3922521	0.135179	-349.2540531
PhEt_pH	-310.7432788	0.123488	-310.6167708
PhEt_pH_TS_haa_by_nsi_rad	-1925.777419	0.305364	-1925.469035
PhEt_pH_TS_haa_by_cu_iii_κ-N	-5267.462844†	0.669215	-5266.790609
PhEt_pH_TS_haa_by_cu_iii_κ-SO	-5267.470967†	0.66779	-5266.800157
nsi_h	-1615.703549	0.172178	-1615.528351
cu_iii_cl_cn_nsi_κ-SO	-4956.733764	0.528631	-4956.202113
sub_1b_TS_haa_by_cu_iii_κ-SO	-5346.066294†	0.720929	-5345.342345
sub_1a_TS_haa_by_cu_iii_κ-SO	-5346.057671†	0.720025	-5345.334626
sub_2b_TS_haa_by_cu_iii_κ-SO	-5385.365109†	0.747347	-5384.614742
sub_2a_TS_haa_by_cu_iii_κ-SO	-5385.355767†	0.7467	-5384.606047
sub_3b_TS_haa_by_cu_iii_κ-SO	-5306.775018†	0.69206	-5306.079938
sub_3a_TS_haa_by_cu_iii_κ-SO	-5306.771207†	0.692431	-5306.075756
tBuO(rad)	-232.9342173	0.090973	-232.8402243
tBuO_h	-233.6107594	0.105438	-233.5023014
sub_1b_TS_haa_by_tBuO(rad)	-622.2680579	0.283144	-621.9818939
sub_1a_TS_haa_by_tBuO(rad)	-622.2664424	0.283325	-621.9800974
sub_2b_TS_haa_by_tBuO(rad)	-661.5643339	0.309355	-661.2519589
sub_2a_TS_haa_by_tBuO(rad)	-661.5618836	0.308837	-661.2500266
sub_3b_TS_haa_by_tBuO(rad)	-582.9735115	0.254561	-582.7159305
sub_3a_TS_haa_by_tBuO(rad)	-582.970743	0.25578	-582.711943
cl(rad)	-460.1300163	-0.015677	-460.1426733
cl_h	-460.8009944	-0.011116	-460.8090904
sub_1b_TS_haa_by_cl(rad)	-849.4830737	0.167144	-849.3129097

†Electronic energies for these broken-symmetry singlet systems are made spin contamination free following the Yamaguchi scheme.

8. Resting state of the •NSI radical

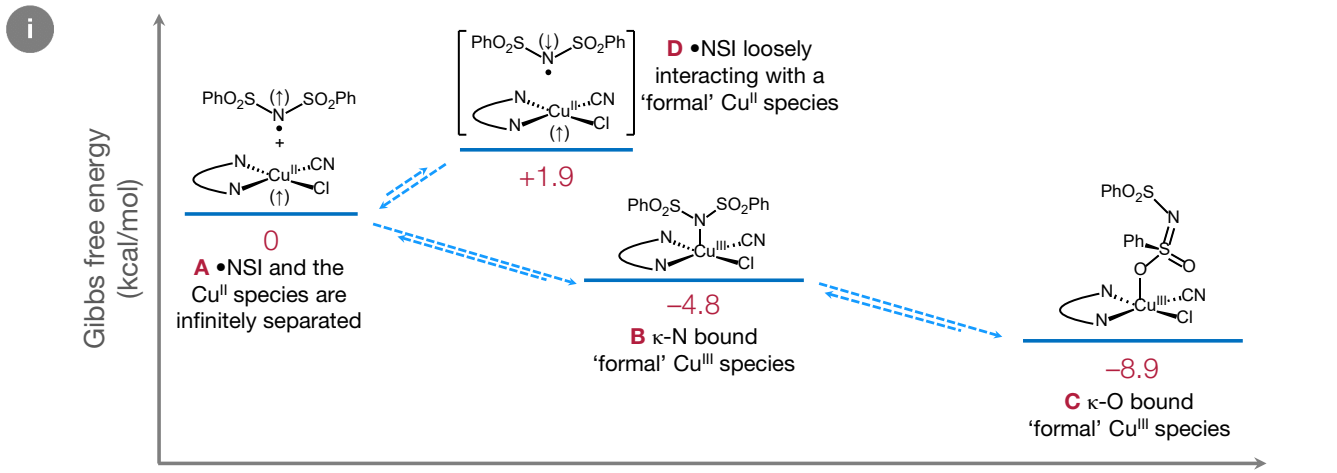

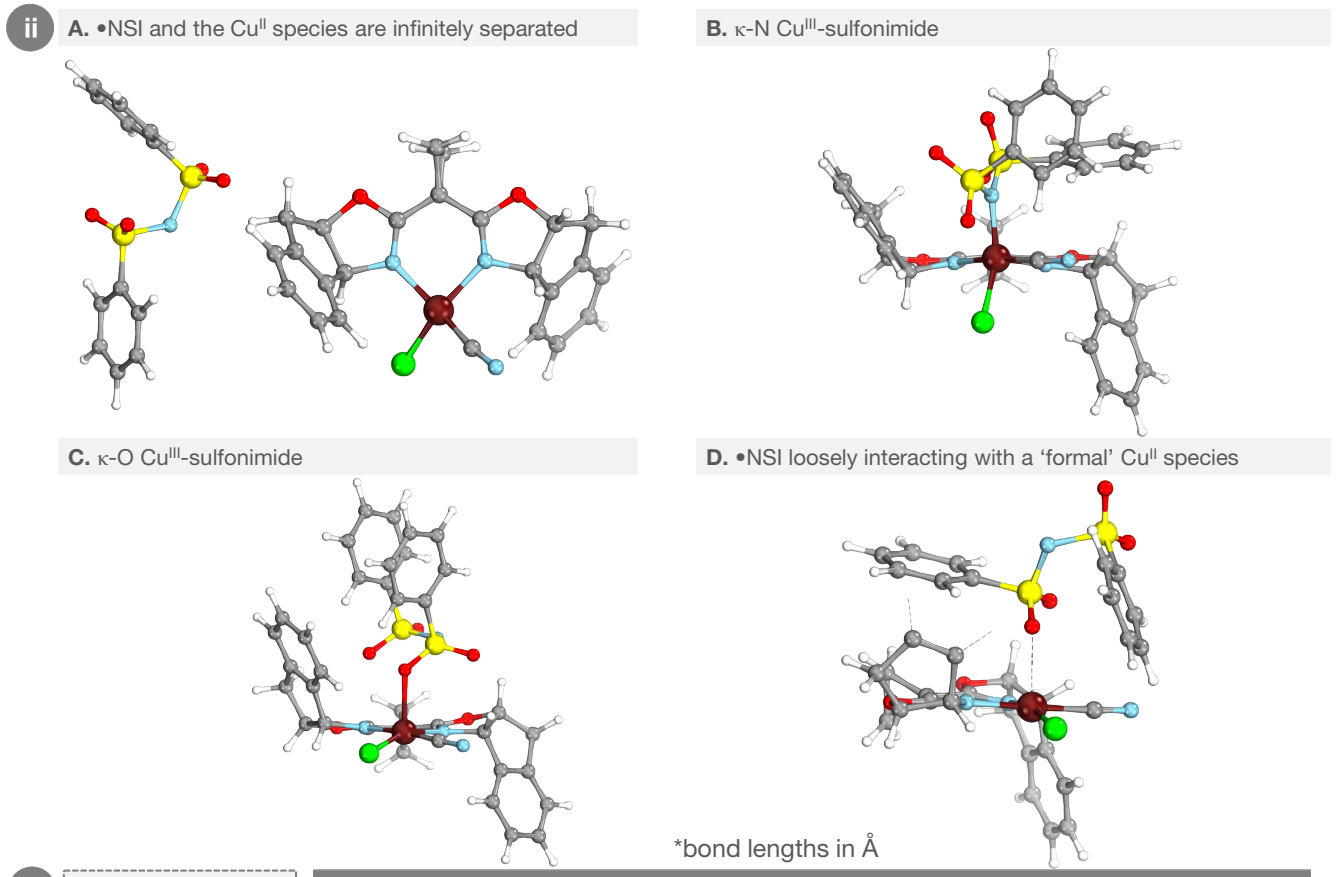

*bond lengths in Å

iii

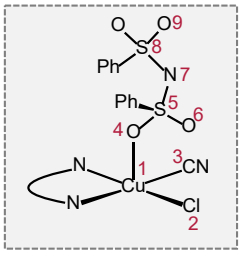

Species	Cu_1–Cl_2	Cu_1–C_3	O_4–S_5	S_5–N_7	N_7–S_8	S_8–O_9	Cu_1–N_7/ Cu_1–O_4
A	2.248	1.938	1.462	1.701	1.715	1.457	–
B	2.218	1.850	1.470	1.655	1.706	1.465	2.017
C	2.184	1.857	1.495	1.611	1.627	1.469	2.241
D	2.291	1.949	1.472	1.682	1.733	1.455	2.404

Figure S9. (i) Energetic comparison of free •NSI and that docked at a Cu^{II} species. Gibbs free energies (kcal/mol) are computed at M06-D3(0)/basis-II/SMD(DCM)//M06-D3(0)/basis-I level of theory at 298.15 K. (ii) Structures of various species (**A**–**D**) relevant to finding the resting state of the •NSI. (iii) Key bond lengths (Ångström) of **A**–**D** are tabulated. Inspection of the O_4–S_5 bond lengths of **A**–**D** (highlighted in red) reveals that it is *longest* in **C**, whereas for S_5–N_7 bond lengths (highlighted in blue), it is *shortest* in **C**.

9. Spin density plots and relative energies of all Cu/NSI species explored

To comprehend the structural and energetic distinctions among the spin-isomers of the κ-N and κ-O Cu/•NSI species examined in this investigation, we conducted a comprehensive exploration of their closed-shell and open-shell singlet, as well as triplet states. The relative energies of these complexes were determined with respect to the isolated $LCu^{II}(Cl)(CN)$ and •NSI species, and the positions of the unpaired spins are depicted in **Figure S10**. Absolute electronic energies and thermal contribution to Gibbs free energies of all six species are depicted in **Table S7**.

(i) κ-N Cu/NSI

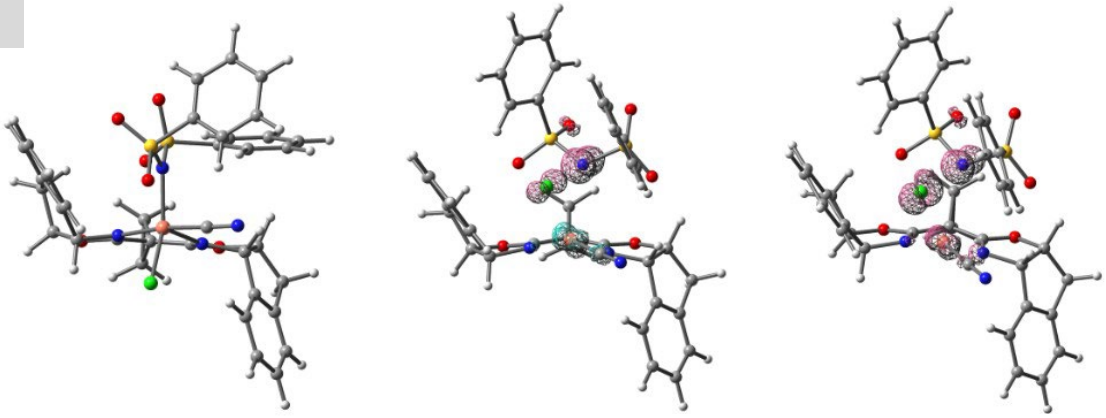

(i-a) restricted singlet
$\Delta G°$ = -4.8 kcal/mol

(i-b) broken-symmetry singlet
$\Delta G°$ = +7.5 kcal/mol

(i-c) triplet
$\Delta G°$ = +5.5 kcal/mol

(ii) κ-O Cu/NSI

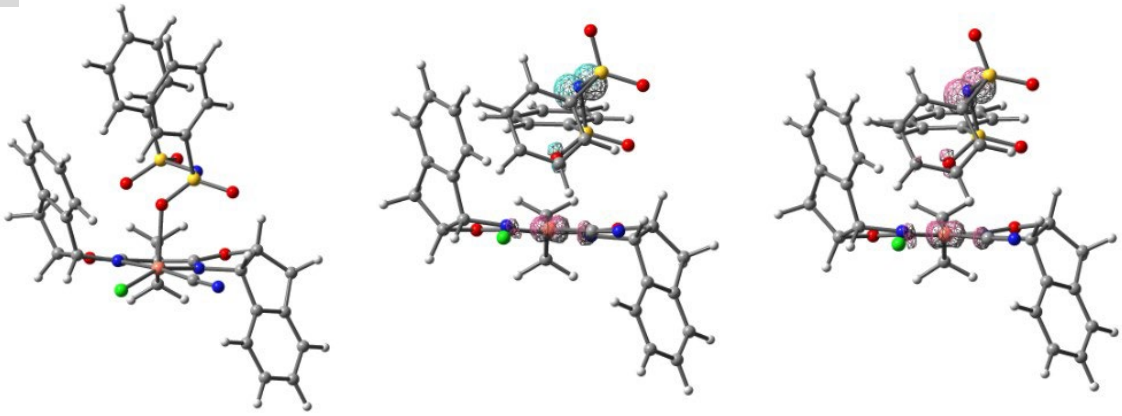

(ii-a) restricted singlet
$\Delta G°$ = -8.9 kcal/mol

(ii-b) broken-symmetry singlet
$\Delta G°$ = +1.9 kcal/mol

(ii-c) triplet
$\Delta G°$ = +1.8 kcal/mol

Figure S10. Spin-isomers of the (i) κ-N Cu/•NSI and (ii) κ-O Cu/•NSI species investigated in this study. The reaction free energies ($\Delta G°$, kcal/mol) are reported by referencing the energy of the isolated $LCu^{II}(Cl)(CN)$ and •NSI species as the *zero* of energy. Using the M06-D3(0)/basis-II/SMD(DCM)//M06-D3(0)/basis-I level of theory at 298.15 K, both κ-N and κ-O isomers exhibited the restricted singlet solutions (i-a) and (ii-a), respectively, as the most energetically favorable conformers. The *α*- and *β*-spins are represented by pink and cyan lobes, respectively.

10. Hydrogen-atom transfer (HAT) vs. proton-coupled electron transfer (PCET)

Two key variations of a hydrogen atom abstraction (HAA) process are described in Figure S11: hydrogen-atom transfer, HAT, where the electron and proton travel "together" between the same donor and acceptor sites, and concerted proton-coupled electron transfer, PCET, where the proton and electron are transferred in parallel, but they do so between different donor and acceptor sites.[11]

An intrinsic bond orbital's (IBO's) change along a reaction coordinate closely follows the "curly arrow", typically used to describe bond-making and bond-breaking processes in a chemical reaction and are particularly valuable for separating HAT from PCET reactions.[11, 12] Accordingly, to distinguish between the operating mechanism(s) during HAA by the free •NSI and the κ-O Cu^{III}-sulfonimide species, we have carried out IBO analysis of the C–H reaction coordinate.

Figure S12(iii–iv) shows evolution of the IBOs of the activated 2° benzylic C–H bond during HAA by free •NSI. We find that the pink lobe representing the *α*-electron of the 2° benzylic C–H bond in Figure S12(iii) evolved into a semilocalized radical on the product, while the blue-green IBO (Figure S12(iv)) representing the *β*-electron of the same C–H bond developed into an N–H bond in H–NSI. Since the electron follows the proton along the HAA reaction coordinate and transfers between the same donor/acceptor sites (Figure S11(i)), the mechanism can be described as an HAT reaction.

A similar analysis was also conducted with the κ-O Cu^{III}-sulfonimide initiator on the same substrate. Figure S13(iii) and Figure S14(ii) show the evolution of the *β*-IBO and *α*-IBO of the C–H bond, respectively, and a comparison between them shows near-identical evolution along the intrinsic reaction coordinate. Considering both the initial C–H IBOs remain on the benzylic substrate along the H-coordinate, an electron must be transferred from another IBO to complete the reaction (recall it is a concerted reaction). Figure S14(iii) shows that it is an α-IBO of the aryl π-cloud of the benzyl substrate that develops into a copper $d_{x^2-y^2}$ orbital near the TS-geometry, indicating direct electron transfer from the substrate to the copper-center. With the transfer of the protons and electrons involving different donor and acceptor centers, this process is best described as a PCET reaction, as indicated with curly arrows in Figure S11(ii).

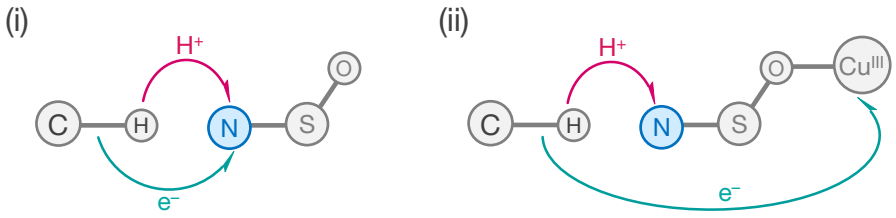

Figure S11. Simplified "curly arrow" description of electron (e^-) and proton (H^+) flow in HAT vs. PCET mediated by free •NSI and κ-O Cu^{III}-sulfonimide species.

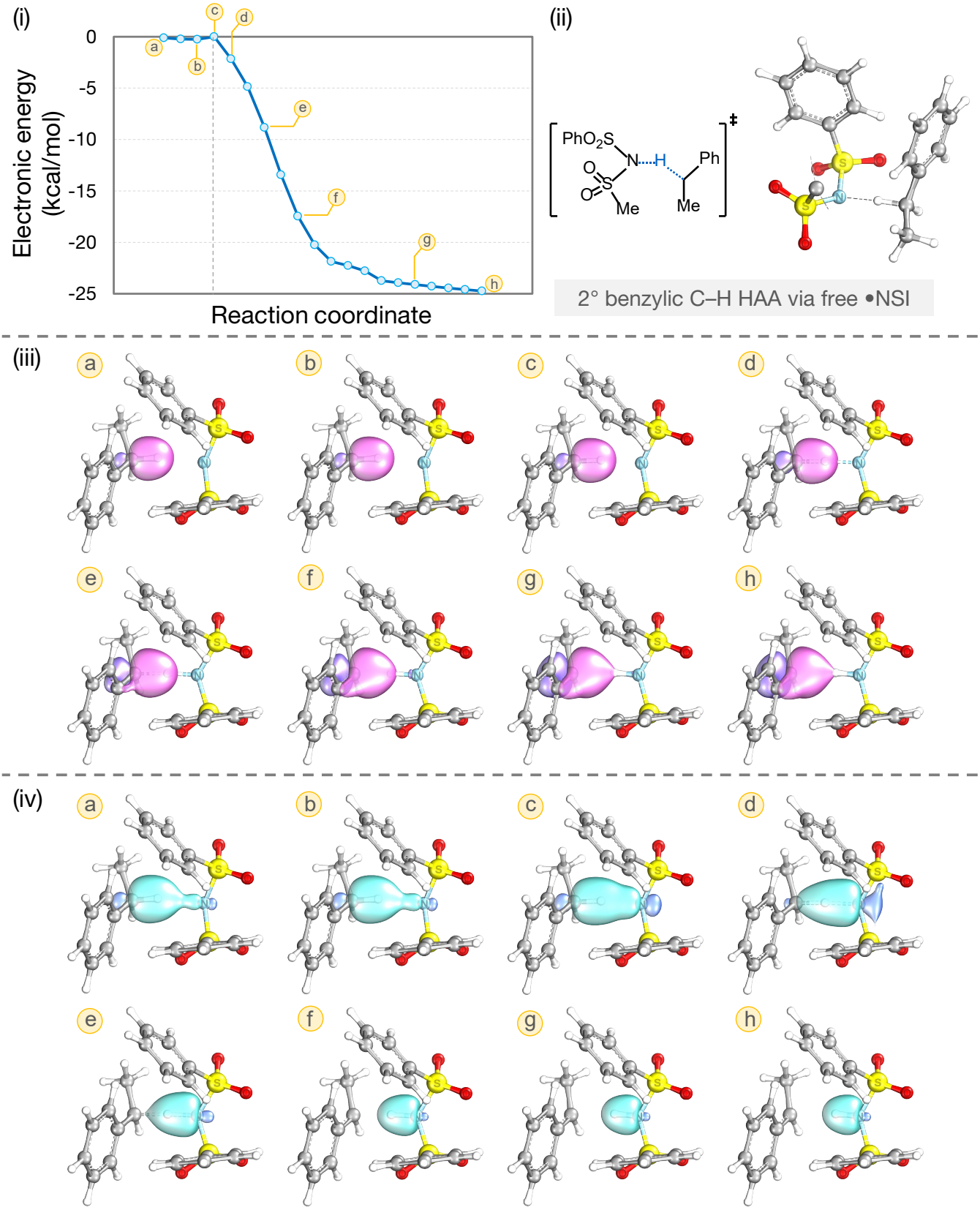

Figure S12. Understanding HAA with the free •NSI radical: (i) Electronic energies (kcal/mol; computed at the M06-D3(0)/basis-I level of theory) along the C–H reaction coordinate (along the potential energy surface, point *a* is "reactant-like", *c* represents the TS, and *h* is "product-like", (ii) depiction of the TS, (iii) IBO transformation along the C–H reaction coordinate for the *α*-IBOs, and (iv) the *β*-IBOs.

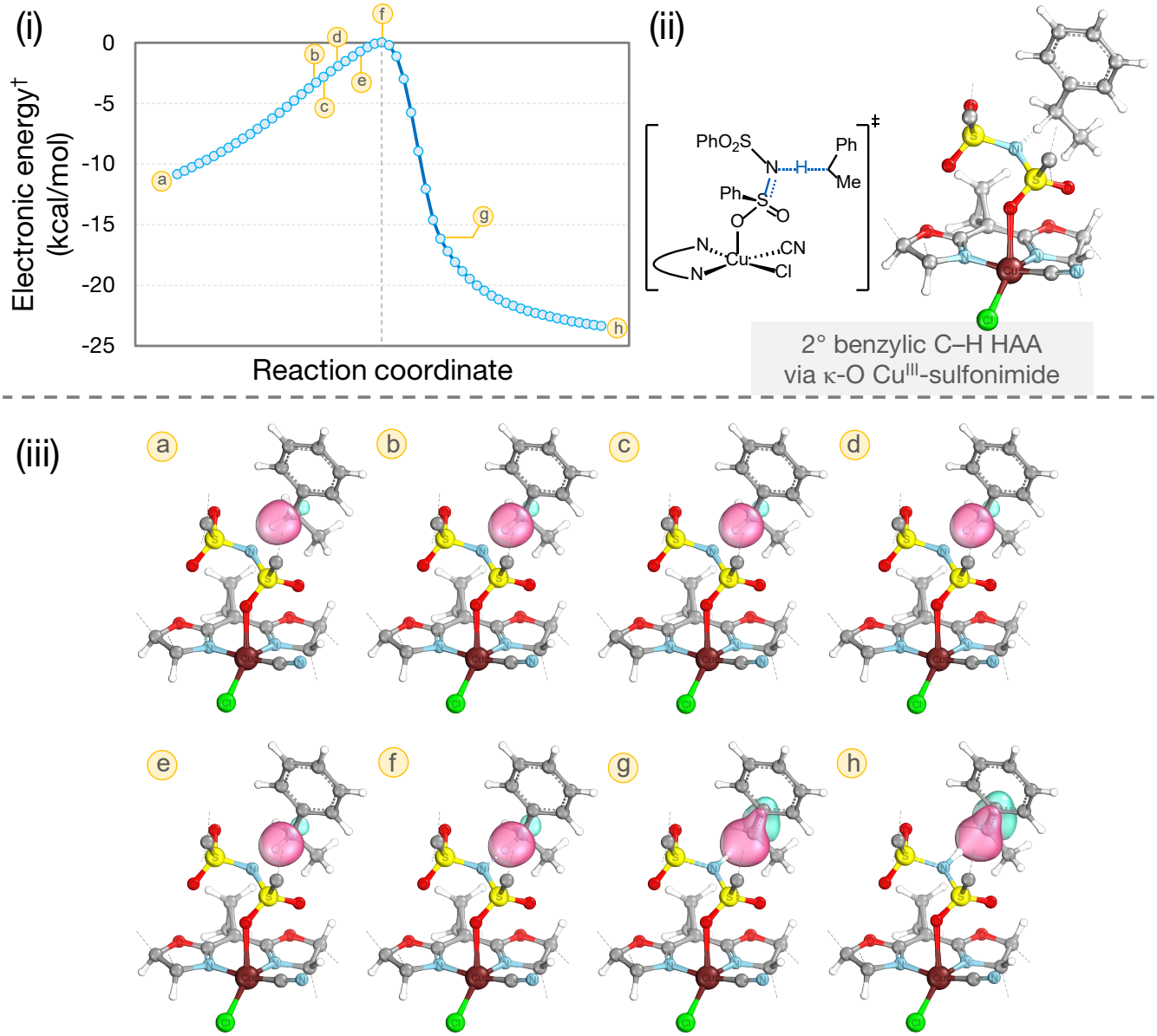

Figure S13. Understanding HAA with the κ-O Cu^{III}-sulfonimide species: (i) Electronic energies (kcal/mol; computed at the M06-D3(0)/basis-I level of theory) along the C–H reaction coordinate (along the potential energy surface, point *a* is "reactant-like", *f* is the TS, and *h* is "product-like", (ii) depiction of the TS, (iii) IBO transformation along the C–H reaction coordinate for the *β*-IBOs of the C–H bond. †Note that the electronic energies reported here do not include the Yamaguchi spin-projection required for a broken symmetry singlet potential energy surface.

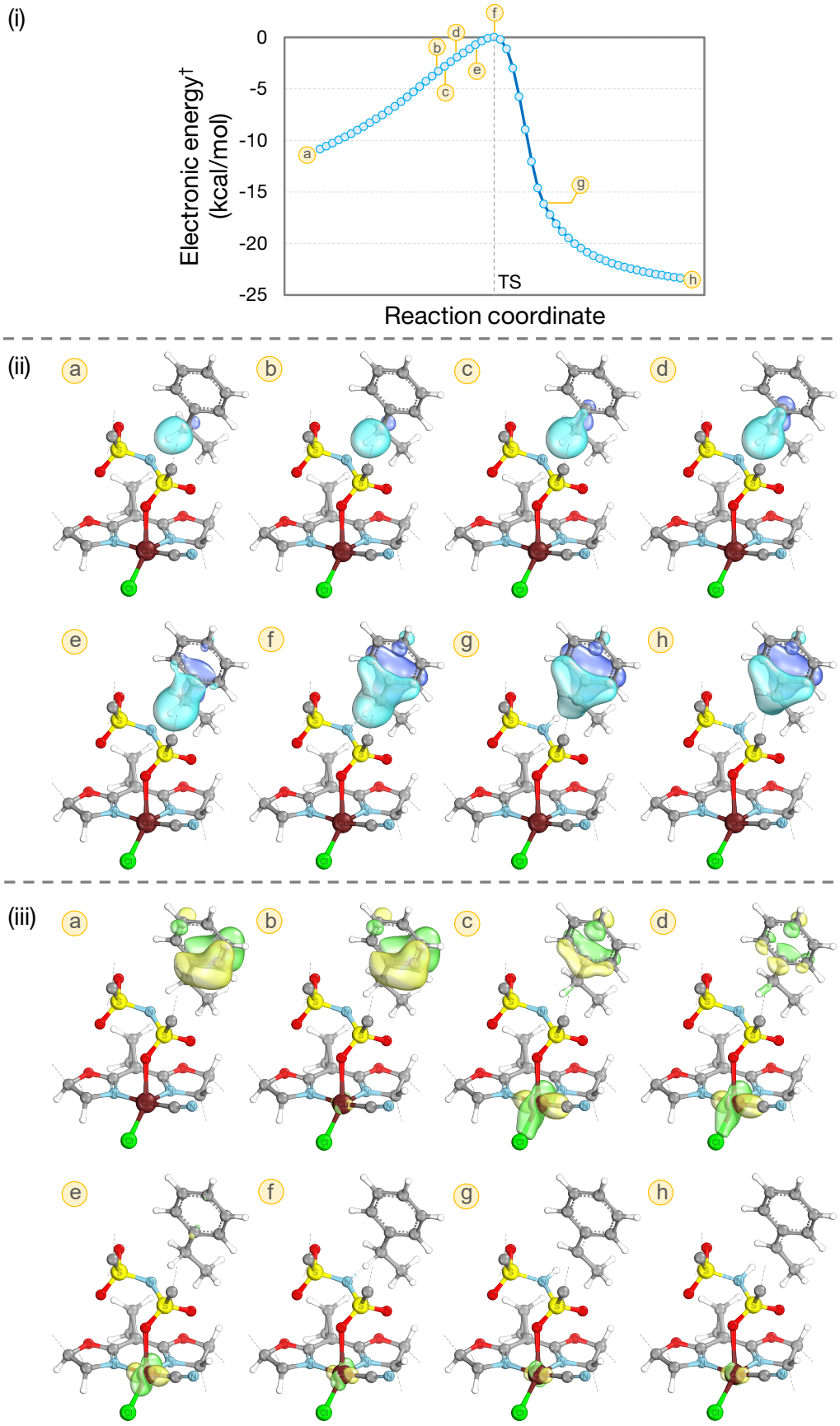

Figure S14. Understanding HAA with the κ-O Cu^{III}-sulfonimide species: (i) Electronic energies along the C–H reaction coordinate; IBO transformation along the C–H reaction coordinate for the (ii) *α*-IBOs of the C–H bond, and the (iii) *α*-IBO of the aryl π-cloud of the benzyl substrate.

11. Computed bond dissociation enthalpies (BDEs)

Table S8. Bond dissociation enthalpies (BDEs) of substrates **1**–**3** as well as of H–Y agents (Y = NSI, O^{t}Bu, Cl). Reaction enthalpies (kcal/mol) are computed at M06-D3(0)/basis-II/SMD(DCM)//M06-D3(0)/basis-I level of theory at 298.15 K. (*a* = aliphatic; *b* = benzylic)

Substrate	Site	BDE (kcal/mol)
1	BDE_{1b}	85.2
	BDE_{1a}	91.8
2	BDE_{2b}	84.4
	BDE_{2a}	92.6
3	BDE_{3b}	83.5
	BDE_{3a}	87.3
H–NSI		107.0
H–O^{t}Bu		103.6
H–Cl		104.0

12. Regioselectivity studies

Table S9. Reaction free energies ($\Delta G°$) for the hydrogen-atom abstraction step involving three HAA initiators described in the text. Gibbs free energies (kcal/mol) are computed at M06-D3(0)/basis-II/SMD(DCM)//M06-D3(0)/basis-I level of theory at 298.15 K. (*a* = aliphatic; *b* = benzylic)

Substrate	$\Delta G°_b$ *vs.* $\Delta G°_a$	κ-O Cu^{III}-sulfonimide	•O^{t}Bu	•Cl
1	$\Delta G°_{1b}$	–12.7	–19.1	–19.5
	$\Delta G°_{1a}$	–6.8	–13.3	–13.7
2	$\Delta G°_{2b}$	–12.9	–19.3	–19.7
	$\Delta G°_{2a}$	–6.4	–12.9	–13.3
3	$\Delta G°_{3b}$	–14.3	–20.7	–21.1
	$\Delta G°_{3a}$	–9.1	–15.5	–15.9

Table S10. Activation free energies ($\Delta G^{\ddagger}$) for the hydrogen-atom abstraction step involving three HAA initiators described in the text. Gibbs free energies (kcal/mol) are computed at M06-D3(0)/basis-II/SMD(DCM)//M06-D3(0)/basis-I level of theory at 298.15 K. (*a* = aliphatic; *b* = benzylic)

Substrate	$\Delta G^{\ddagger}_b$ *vs.* $\Delta G^{\ddagger}_a$	κ-O Cu^{III}-sulfonimide	•O^{t}Bu	•Cl
1	$\Delta G^{\ddagger}_{1b}$	10.9	10.0	–8.0
	$\Delta G^{\ddagger}_{1a}$	15.7	11.1	--
2	$\Delta G^{\ddagger}_{2b}$	10.1	10.6	--
	$\Delta G^{\ddagger}_{2a}$	15.5	11.9	--
3	$\Delta G^{\ddagger}_{3b}$	8.9	10.2	--
	$\Delta G^{\ddagger}_{3a}$	11.5	12.7	--

13. Steric maps for comparing reactivity at aliphatic vs. benzylic C–H bonds

When considering the reactivity and selectivity between aliphatic and benzylic C–H bonds, the steric factors originating from the Cu/•NSI adduct are expected to play an important role. Generally, these factors are anticipated to favor reactivity at the 2° benzylic sites over the 3° aliphatic sites. To evaluate the influence of the steric profile on the reactivity, we calculated the fractional buried volume (% V_{Bur}).[13] This parameter quantitatively characterizes the steric environment within a given catalytic pocket. The % V_{Bur} values for the relevant transition state structures involving the reactivity at the benzylic and aliphatic positions of substrate **1** with κ-O Cu/•NSI are depicted in **Figure S15**. The benzylic reactivity of substrate **1** with κ-O Cu/•NSI exhibits a slightly higher amount of 'free' space (approximately 10%) compared to the aliphatic case (approximately 7.6%), confirming reduced steric hindrance to the reactivity.

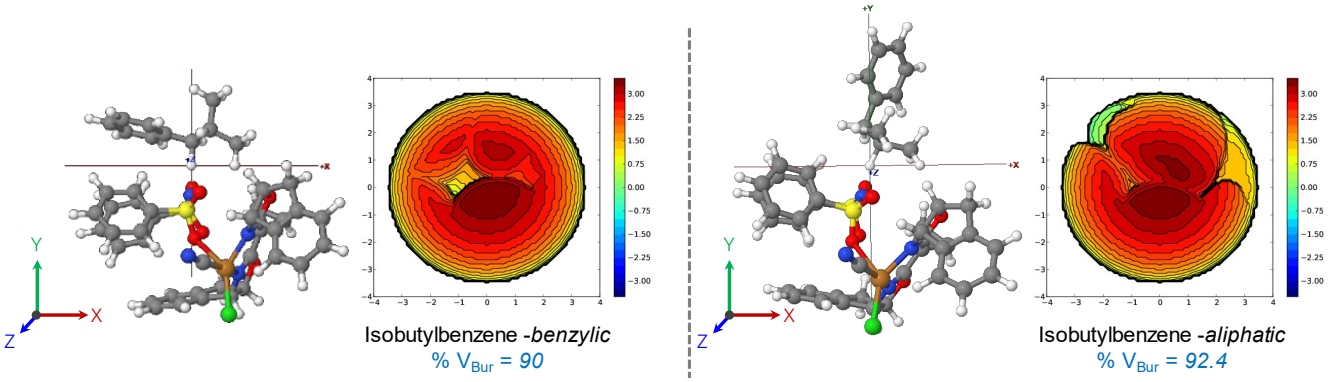

Figure S15. The fractional buried volume (% V_{Bur}), calculated by considering a 3.5 Å sphere surrounding the abstracted *H* atom, indicates that the benzylic reactivity of substrate **1** with κ-O Cu/•NSI exhibits a lower steric hindrance, as evidenced by a higher percentage of free space (~ 10%) compared to the aliphatic case (~ 7.6%).

14. Energetics for product forming pathways: Cyanation vs. azidation vs. etherification

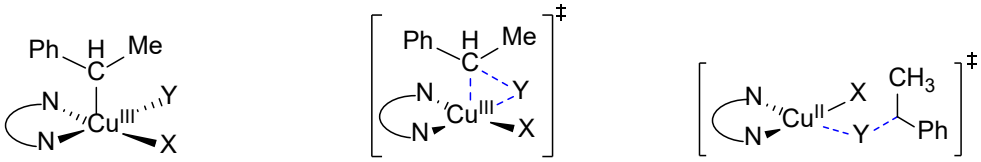

X =	Y =	file_name	file_name	file_name
Cl	CN	R_org_met_RE_preTS_int_cl_cn	R_org_met_RE_TS_cl_cn	R_RAL_TS_broken_sym_cl_cn
CN	CN	R_org_met_RE_preTS_int_cn_cn	R_org_met_RE_TS_cn_cn	R_RAL_TS_broken_sym_cn_cn
Cl	N_3	R_org_met_RE_preTS_int_cl_n3	R_org_met_RE_TS_cl_n3	R_RAL_TS_broken_sym_cl_n3
Cl	OMe	R_org_met_RE_preTS_int_cl_ome	R_org_met_RE_TS_cl_ome	R_RAL_TS_broken_sym_cl_ome
NSI	CN	R_org_met_RE_preTS_int_nsi_cn	R_org_met_RE_TS_nsi_cn	R_RAL_TS_broken_sym_nsi_cn
NSI	N_3	R_org_met_RE_preTS_int_nsi_n3	R_org_met_RE_TS_nsi_n3	R_RAL_TS_broken_sym_nsi_n3
NSI	OMe	R_org_met_RE_preTS_int_nsi_ome	R_org_met_RE_TS_nsi_ome	R_RAL_TS_broken_sym_nsi_ome

Figure S16. Line drawing of a generic reductive elimination (RE) transition state (TS) structure, a typical 'formally' LCu^{III} intermediate that precedes the RE TS structure, and the TS describing direct radical addition at a copper-bound ligand. The corresponding energetics are shown in **Table S11**.

.

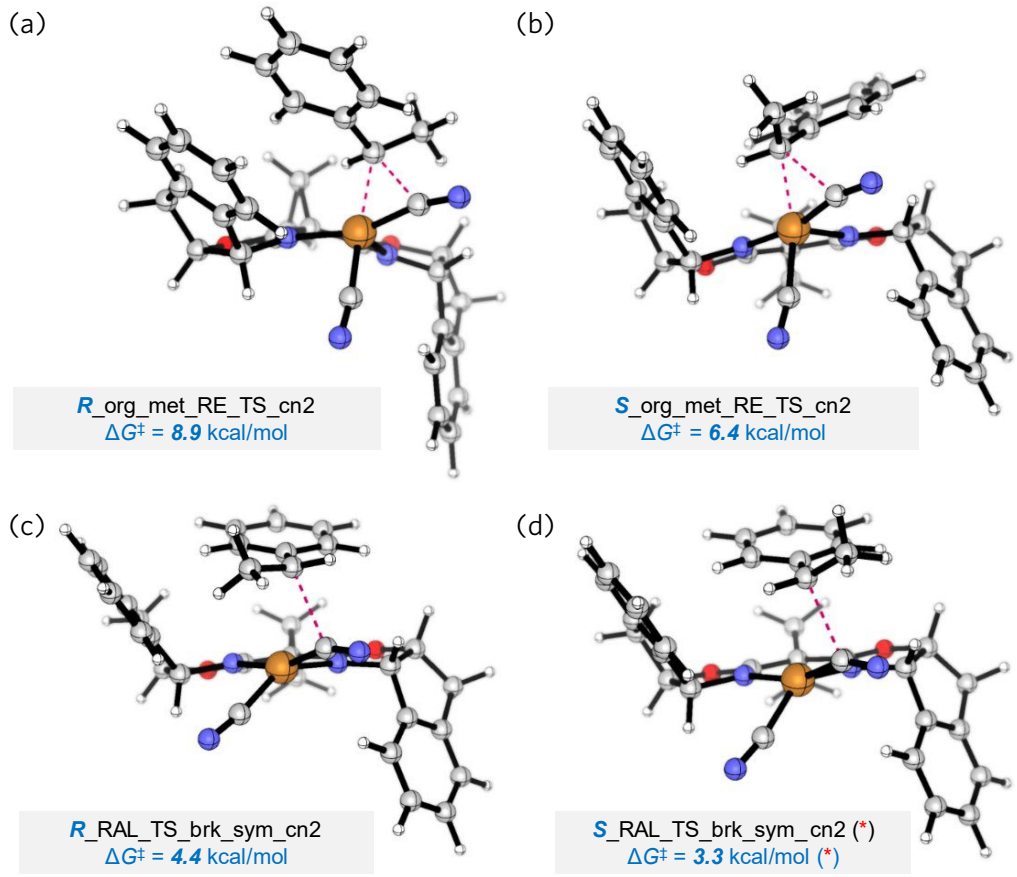

Figure S17. Exploring enantioselectivity during cyanation of $PhCH_2Me$. Both reductive elimination (RE) and radical addition to ligand (RAL) favor formation of the *S*-stereoisomer, although RAL is shown to have a lower overall barrier. The activation free energies ($\Delta G^{\ddagger}$) are reported with reference to the energy of the spin-triplet precomplex of $LCu^{II}(CN)(CN)$ and $PhCH(\bullet)Me$ species set as the *zero* energy point. Gibbs free energies are reported in kcal/mol and calculated using the M06-D3(0)/basis-II/SMD(DCM)//M06-D3(0)/basis-I level of theory at 298.15 K. The corresponding (absolute) energetics are shown in **Table S11**. *Not all convergence criterions were fulfilled during optimization of this transition state structure.

Table S11. Electronic energies, Gibbs free energies (G) and thermal contribution to G for structures shown in **Figure S16**. Energies are reported in hartree computed at M06-D3(0)/basis-II/SMD(DCM)//M06-D3(0)/basis-I level of theory at 298.15 K.

File/Structure name	Electronic energy (hartree)	Thermal contribution to *G* (hartree)	Gibbs free energy (*G*, hartree)
R_org_met_RE_preTS_int_cl_cn	-3651.782292	0.474969	-3651.304303
R_org_met_RE_preTS_int_cn_cn	-3284.360129	0.479436	-3283.877673
R_org_met_RE_preTS_int_cl_n3	-3723.137682	0.47818	-3722.656482
R_org_met_RE_preTS_int_cl_ome	-3674.054901	0.506292	-3673.545589
R_org_met_RE_preTS_int_nsi_cn	-4806.681652	0.666489	-4806.012143
R_org_met_RE_preTS_int_nsi_n3	-4878.042087	0.668504	-4877.370563
R_org_met_RE_preTS_int_nsi_ome	-4828.959756	0.698267	-4828.258469
R_org_met_RE_TS_cl_cn	-3651.776552	0.474027	-3651.299505

R_org_met_RE_TS_cn_cn	-3284.355919	0.479279	-3283.87362
R_org_met_RE_TS_cl_n3	-3723.128687	0.475137	-3722.65053
R_org_met_RE_TS_cl_ome	-3674.041434	0.50067	-3673.537744
R_org_met_RE_TS_nsi_cn	-4806.678548	0.665434	-4806.010094
R_org_met_RE_TS_nsi_n3	-4878.037236	0.665995	-4877.368221
R_org_met_RE_TS_nsi_ome	-4828.949366	0.696407	-4828.249939
R_RAL_preTS_int_triplet_cl_cn	-3651.785369	0.467903	-3651.314446
R_RAL_preTS_int_triplet_cn_cn	-3284.364505	0.473745	-3283.88774
R_RAL_preTS_int_triplet_cl_n3	-3723.150862	0.473734	-3722.674108
R_RAL_preTS_int_triplet_cl_ome	-3674.068042	0.5018	-3673.563222
R_RAL_preTS_int_triplet_nsi_cn	-4806.681073	0.659247	-4806.018806
R_RAL_preTS_int_triplet_nsi_n3	-4878.047004	0.664675	-4877.379309
R_RAL_preTS_int_triplet_nsi_ome	-4828.963295	0.693039	-4828.267236
R_RAL_TS_brk_sym_cl_cn	-3651.781326†	0.471427	-3651.306879
R_RAL_TS_brk_sym_cn_cn	-3284.360997†	0.477254	-3283.880723
R_RAL_TS_brk_sym_cl_n3_N-alph	-3723.146215†	0.473436	-3722.669759
R_RAL_TS_brk_sym_cl_n3_N-gam	-3723.139703†	0.474854	-3722.661829
R_RAL_TS_brk_sym_cl_ome	-3674.067713†	0.502705	-3673.561988
R_RAL_TS_brk_sym_nsi_cn≠	-4806.678555†	0.661503	-4806.014032
R_RAL_TS_brk_sym_nsi_n3_N-alph	-4878.044883†	0.664031	-4877.377832
R_RAL_TS_brk_sym_nsi_n3_N-gam	-4878.041901†	0.66542	-4877.373461
R_RAL_TS_brk_sym_nsi_ome	-4828.966864†	0.694022	-4828.269822
cuii_cn2_ph_CHMeRad_INT_triplet	-3284.364505	0.473745	-3283.88774
R_org_met_RE_TS_cn_cn	-3284.355923	0.479278	-3283.873625
S_org_met_RE_TS_cn_cn	-3284.360922	0.480353	-3283.877549
R_RAL_TS_cn_cn_brk_sym	-3284.360996†	0.4772540	-3283.880723
S_RAL_TS_cn_cn_brk_sym≠	-3284.362045†	0.4765550	-3283.8824701

†Electronic energies for these broken-symmetry singlet TSs are made spin contamination free following the Yamaguchi scheme. ≠Not all convergence criterions were met during optimization of this structure.

15. Comparing Cu/NFSI reactivity with analogous methods yielding benzylic cation

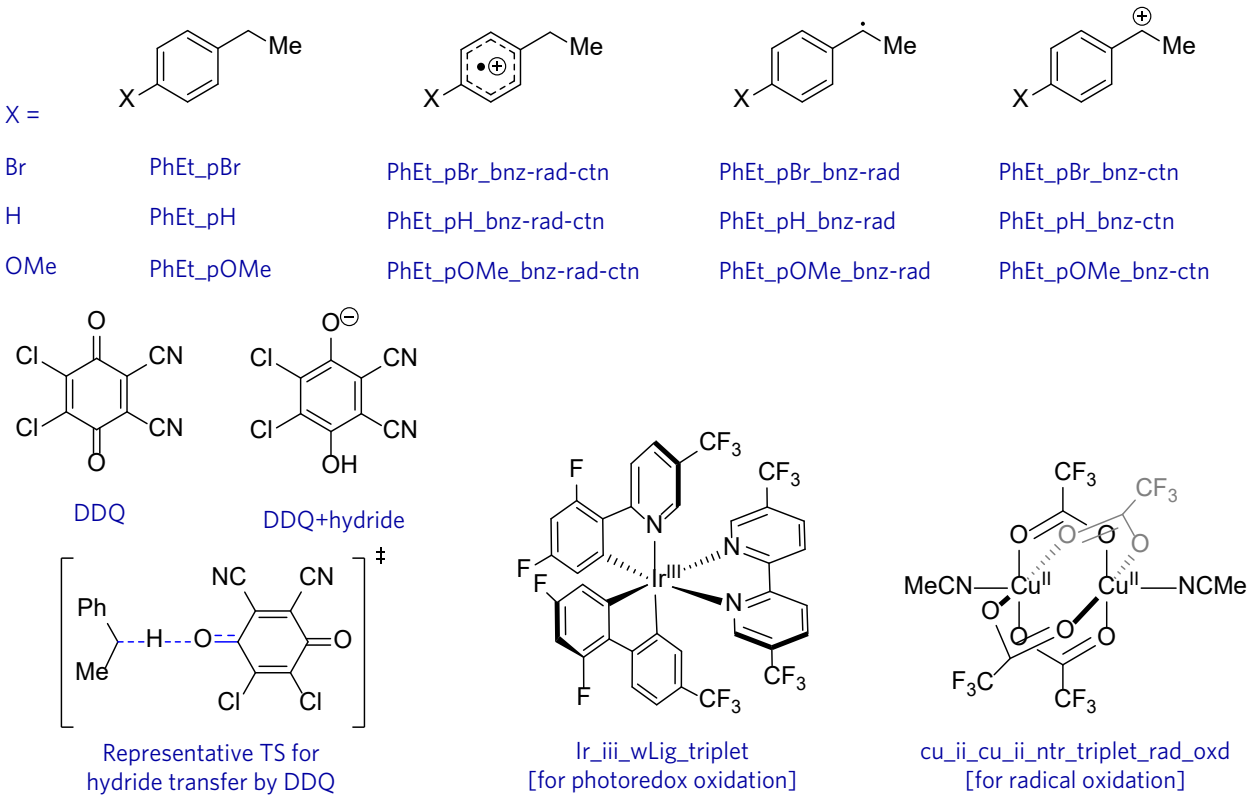

Figure S18. Line drawing of the structures, the energetics of which are shown in **Table S12.**

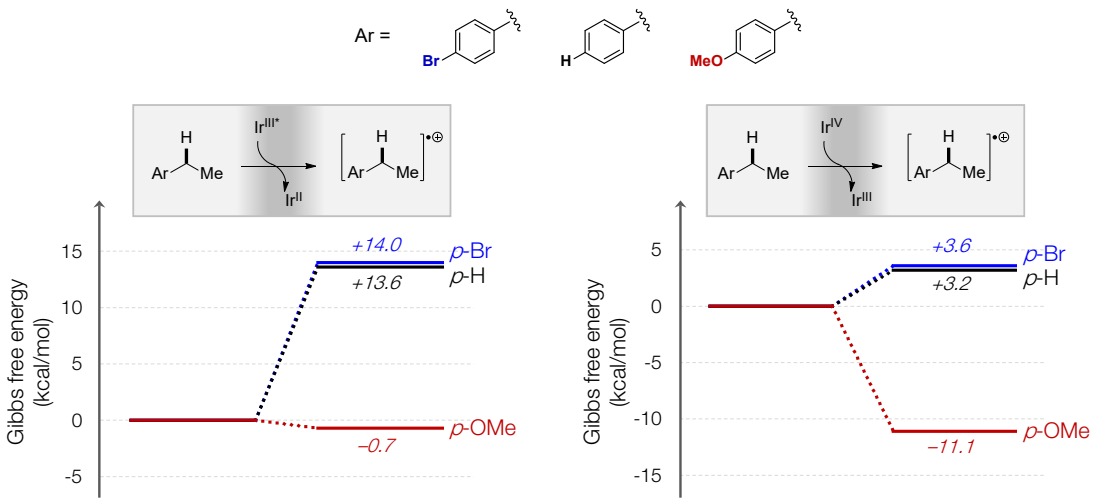

Figure S19. Comparing radical cation generation from benzylic C–H substrate using Ir^{III*} *vs* Ir^{IV} catalysts, the raw energetics of which are shown in **Table S12**.

Table S12. Electronic energies, Gibbs free energies (G) and thermal contribution to G for structures shown in **Figure S18** and **Figure S19**. Energies are reported in hartree computed at M06-D3(0)/basis-II/SMD(DCM)//M06-D3(0)/basis-I level of theory at 298.15 K.

File/Structure name	Electronic energy (hartree)	Thermal contribution to G (hartree)	Gibbs free energy (G, hartree)
PhEt_pBr	-2884.214511	0.110159	-2884.101332
PhEt_pH	-310.7432788	0.123488	-310.6167708
PhEt_pOMe	-425.252048	0.152468	-425.09656
PhEt_pBr_bnz-rad-ctn	-2883.976883	0.108157	-2883.865706
PhEt_pH_bnz-rad-ctn	-310.5049956	0.120144	-310.3818316
PhEt_pOMe_bnz-rad-ctn	-425.0386741	0.151214	-424.8844401
PhEt_pBr_bnz-rad	-2883.570219	0.096	-2883.471199
PhEt_pH_bnz-rad	-310.0983805	0.108854	-309.9865065
PhEt_pOMe_bnz-rad	-424.6078587	0.137652	-424.4671867
PhEt_pBr_bnz-ctn	-2883.395874	0.0991	-2883.293754
PhEt_pH_bnz-ctn	-309.928007	0.112355	-309.812632
PhEt_pOMe_bnz-ctn	-424.4532553	0.142345	-424.3078903
cu_iii_cl_cn_nsi_κ-SO	-4956.733764	0.528631	-4956.202113
cu_ii_cl_cn_wLig	-3341.664771	0.335583	-3341.326168
nsi_h	-1615.703549	0.172178	-1615.528351
PhEt_pBr_TS_haa_by_cu_iii_κ-SO	-7840.941955[†]	0.655315	-7840.28362
PhEt_pH_TS_haa_by_cu_iii_κ-SO	-5267.470967[†]	0.66779	-5266.800157
PhEt_pOMe_TS_haa_by_cu_iii_κ-SO	-5381.993554[†]	0.700134	-5381.2904
DDQ	-1484.983215	0.023427	-1484.956768
DDQ+hydride	-1485.774668	0.035351	-1485.736297
PhEt_pBr_TS_hydride_shift_ddq	-4369.175182	0.154686	-4369.017476
PhEt_pH_TS_hydride_shift_ddq	-1795.705413	0.167581	-1795.534812
PhEt_pOMe_TS_hydride_shift_ddq	-1910.223696	0.196804	-1910.023872
Ir_iv_wLig	-3301.788396	0.388244	-3301.397132
Ir_iii_wLig_triplet	-3301.937626	0.385651	-3301.548955
Ir_iii_wLig_singlet	-3302.01964	0.389628	-3301.626992
Ir_ii_wLig	-3302.151565	0.386353	-3301.762192
cu_ii_cu_ii_ntr_singlet_rad_oxd	-5651.464383	0.134163	-5651.3272
cu_ii_cu_ii_ntr_triplet_rad_oxd	-5651.512982	0.135447	-5651.374515
cu_ii_cu_i_ann_doublet_rad_oxd	-5651.679733	0.136059	-5651.540654
K2HPO4	-1842.986951	-0.007497	-1842.991428
K2HPO4+(H+)	-1843.458761	0.003759	-1843.451982

[†]Electronic energies for these broken-symmetry singlet TSs are made spin contamination free following the Yamaguchi scheme.

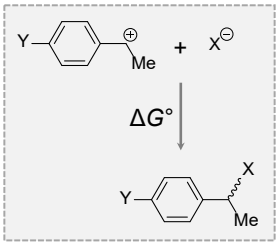

ΔG° (kcal/mol)	Y = Br	Y = H	Y = OMe
X = CN	–61.9	–60.3	–51.1
X = N_3	–47.7	–46.0	–36.7
X = OMe	–78.6	–76.5	–67.2

Figure S20. Schematic for benzylic carbocation trapping by a nucleophile. Reaction free energies (Δ*G*°, kcal/mol) for trapping a benzylic carbocation by different nucleophiles (X = CN, N_3, OMe) and with various para substituents on the benzyl cation substrate (Y = Br, H, OMe) were calculated at 298.15 K using the M06-D3(0)/basis-II/SMD(DCM)//M06-D3(0)/basis-I level of theory.

Table S13. Electronic energies, Gibbs free energies (*G*) and thermal contribution to *G* for structures shown in **Figure S20.** Energies are reported in hartree computed at M06-D3(0)/basis-II/SMD(DCM)//M06-D3(0)/basis-I level of theory at 298.15 K.

File/Structure name	Electronic energy (hartree)	Thermal contribution to *G* (hartree)	Gibbs free energy (*G*, hartree)
PhEt_pBr_bnz-ctn	-2883.395874	0.099100	-2883.293754
PhEt_pH_bnz-ctn	-309.928007	0.112355	-309.812632
PhEt_pOMe_bnz-ctn	-424.453255	0.142345	-424.307890
cyanide_anion	-92.9225879	-0.014065	-92.9336329
azide_anion	-164.2910419	-0.005229	-164.2932509
methoxide_anion	-115.1754287	0.014324	-115.1580847
Ar_CH(CN)_Me (p-Br)	-2976.435888	0.106783	-2976.3260858
Ar_CH(CN)_Me (p-H)	-402.9654835	0.120144	-402.8423195
Ar_CH(CN)_Me (p-OMe)	-517.4750910	0.149090	-517.3229810
Ar_CH(N3)_Me (p-Br)	-3047.776247	0.110205	-3047.6630222
Ar_CH(N3)_Me (p-H)	-474.3055700	0.123342	-474.1792080
Ar_CH(N3)_Me (p-OMe)	-588.8154078	0.152829	-588.6595588
Ar_CH(OMe)_Me (p-Br)	-2998.719549	0.139483	-2998.5770462
Ar_CH(OMe)_Me (p-H)	-425.2485005	0.152817	-425.0926635
Ar_CH(OMe)_Me (p-OMe)	-539.7578943	0.181775	-539.5730993

16. References

(1) Hu, H.; Chen, S.-J.; Mandal, M.; Pratik, S. M.; Buss, J. A.; Krska, S. W.; Cramer, C. J.; Stahl, S. S. Copper-catalysed benzylic C–H coupling with alcohols via radical relay enabled by redox buffering. *Nat. Catal.* **2020**, *3*, 358–367. https://doi.org/10.1038/s41929-020-0425-1.

(2) Lopez, M. A.; Buss, J. A.; Stahl, S. S. Cu-Catalyzed Site-Selective Benzylic Chlorination Enabling Net C–H Coupling with Oxidatively Sensitive Nucleophiles. *Org. Lett.* **2022**, *24*, 597–601. https://doi.org/10.1021/acs.orglett.1c04038.

(3) Ozawa, J.; Kanai, M. Silver-Catalyzed C(sp^3)–H Chlorination. *Org. Lett.* **2017**, *19*, 1430–1433. https://doi.org/10.1021/acs.orglett.7b00367.

(4) Bruker-AXS (2016). *APEX3*. Version 2016.5-0. Madison, Wisconsin, USA.

(5) Krause, L.; Herbst-Irmer, R.; Sheldrick, G. M.; Stalke, D. Comparison of Silver and Molybdenum Microfocus X-Ray Sources for Single-Crystal Structure Determination. *J. Appl. Cryst.* **2015**, *48*, 3–10. https://doi.org/10.1107/S1600576714022985.

(6) (a) Sheldrick, G. M. (2013b). *XPREP*. Version 2013/1. Georg-August-Universität Göttingen, Göttingen, Germany. (b) Sheldrick, G. M. (2013a). The *SHELX* homepage, https://shelx.uni-goettingen.de/ (accessed on Jan 03, 2023).

(7) (a) Sheldrick, G. SHELXT - Integrated Space-Group and Crystal-Structure Determination. *Acta Crystallogr. Sect. A* **2015**, *71*, 3–8. https://doi.org/10.1107/S2053273314026370 (b) Sheldrick, G. Crystal Structure Refinement with SHELXL. *Acta Crystallogr. Sect. C* **2015**, *71*, 3–8. https://doi.org/10.1107/S2053229614024218.

(8) Dolomanov, O. V; Bourhis, L. J.; Gildea, R. J.; Howard, J. A. K.; Puschmann, H. OLEX2: A Complete Structure Solution, Refinement and Analysis Program. *J. Appl. Crystallogr.* **2009**, *42*, 339–341. https://doi.org/10.1107/S0021889808042726.

(9) Guzei, I. A. (2007–2013). Programs *Gn*. University of Wisconsin-Madison, Madison, Wisconsin, USA.

(10) Spek, A. PLATON SQUEEZE: A Tool for the Calculation of the Disordered Solvent Contribution to the Calculated Structure Factors. *Acta Crystallogr. Sect. C* **2015**, *71*, 9–18. https://doi.org/10.1107/S2053229614024929.

(11) (a) Mandal, M.; Elwell, C. E.; Bouchey, C. J.; Zerk, T. J.; Tolman, W. B.; Cramer, C. J. Mechanisms for Hydrogen-Atom Abstraction by Mononuclear Copper(III) Cores: Hydrogen-Atom Transfer or Concerted Proton-Coupled Electron Transfer? *J. Am. Chem. Soc.* **2019**, *141*, 17236–17244. https://doi.org/10.1021/jacs.9b08109. (b) Elwell, C. E.; Mandal, M.; Bouchey, C. J.; Que, L.; Cramer, C. J.; Tolman, W. B. Carboxylate Structural Effects on the Properties and Proton-Coupled Electron Transfer Reactivity of $[CuO_2CR]^{2+}$ Cores. *Inorg. Chem.* **2019**, *58*, 15872–15879.
https://doi.org/10.1021/acs.inorgchem.9b02293. (c) Mandal, M.; Cramer, C. J.; Truhlar, D. G.; Sauer, J.; Gagliardi, L. Structure and Reactivity of Single-Site Vanadium Catalysts Supported on Metal–Organic Frameworks. *ACS Catal.* **2020**, *10*, 10051–10059. https://doi.org/10.1021/acscatal.0c02300.

(12) Klein, J. E. M. N.; Knizia, G. cPCET versus HAT: A Direct Theoretical Method for Distinguishing X–H Bond-Activation Mechanisms. *Angew. Chem. Int. Ed.* **2018**, *57*, 11913–11917. https://doi.org/10.1002/anie.201805511.

(13) (a) Falivene, L.; Cao, Z.; Petta, A.; Serra, L.; Poater, A.; Oliva, R.; Scarano, V.; Cavallo, L. Towards the Online Computer-Aided Design of Catalytic Pockets. *Nat. Chem.* **2019**, *11*, 872–879. https://doi.org/10.1038/s41557-019-0319-5 (b) Falivene, L.; Credendino, R.; Poater, A.; Petta, A.; Serra, L.; Oliva, R.; Scarano, V.; Cavallo, L. SambVca 2. A Web Tool for Analyzing Catalytic Pockets with Topographic Steric Maps. Organometallics 2016, 35, 2286– 2293. DOI: 10.1021/acs.organomet.6b00371 (c) Macaranas, J. A.; Luke, A. M.; Mandal, M.; Neisen, B. D.; Marell, D. J.; Cramer, C. J.; Tolman, W. B. Sterically Induced Ligand Framework Distortion Effects on Catalytic Cyclic Ester Polymerizations. *Inorg. Chem.* **2018**, *57*, 3451–3457. https://doi.org/10.1021/acs.inorgchem.8b00250.